

# REPORT DOCUMENTATION PAGE

Form Approved  
OMB No. 0704-0188

Public reporting burden for this collection of information is estimated to average 1 hour per response, including the time for reviewing instructions, searching existing data sources, gathering and maintaining the data needed, and completing and reviewing the collection of information. Send comments regarding this burden estimate or any other aspect of this collection of information, including suggestions for reducing this burden, to Washington Headquarters Services, Directorate for Information Operations and Reports, 1215 Jefferson Davis Highway, Suite 1204, Arlington, VA 22202-4302, and to the Office of Management and Budget, Paperwork Reduction Project (0704-0188), Washington, DC 20503.

|  |  |   |                            |   |  |
|--|--|---|----------------------------|---|--|
| 1. AGENCY USE ONLY (Leave blank)   |  | 2. REPORT DATE<br>3 Apr 97                              |                            | 3. REPORT TYPE AND DATES COVERED<br>Final 1 Mar 95 - 31 Dec 96        |  |
| 4. TITLE AND SUBTITLE<br>Nonlinear Rheology Of Rock At Moderate Strains And Its Importance To Discrimination, Detection, And Yield Estimation Of Underground Explosions  |  |   |                            | 5. FUNDING NUMBERS<br>C F49620-95-C-0019<br>PR 2309                   |  |
| 6. AUTHOR(S)<br>Greg N. Boitnott   |  |   |                            |   |  |
| 7. PERFORMING ORGANIZATION NAME(S) AND ADDRESS(ES)<br>New England Research, Inc.<br>76 Olcott Drive<br>White River Junction, VT 05001  |  |   |                            |   |  |
| 9. SPONSORING/MONITORING AGENCY NAME(S) AND ADDRESS(ES)<br>Air Force Office of Scientific Research<br>110 Duncan Avenue Suite B115<br>Bolling AFB DC 20332-0001  |  |   |                            | 10. SPONSORING/MONITORING AGENCY REPORT NUMBER<br>AFOSR-TR-97<br>0195 |  |
| 11. SUPPLEMENTARY NOTES  |  |   |                            |   |  |
| 12a. DISTRIBUTION/AVAILABILITY STATEMENT<br>Unlimited  |  |   |                            | 12b. DISTRIBUTION CODE<br>DTIC QUALITY INSPECTED 2                    |  |
| 13. ABSTRACT (Maximum 200 words)<br><p>A laboratory experimental program has been performed to characterize the rheology of rock subject to moderate perturbations in stress. The objectives were to provide laboratory data to aid in the development and constraint of realistic rock rheologies suitable for modeling wave propagation in the moderate-strain and brittle-damage regimes. This information was needed to better understand the extent to which nonlinear material properties are important to regional discriminants and event detection.</p> <p>Experiments were performed to characterize the intrinsic loading path dependence of the deformation of rock subjected to various loading conditions. Cyclic loading tests involving unconfined uniaxial compression, torsion, hydrostatic compression, confined uniaxial compression, uniaxial strain, confined shear stress, and explosion-like loading paths were conducted on a variety of lithologies under conditions expected in the moderate-strain and brittle-damage regimes of an underground explosion. The data clearly illustrate nonlinearities even at stress conditions which might typically be considered outside the elastic radius of a seismic event. A rheology is developed suitable for forward modeling of wave propagation through the moderate strain regime.</p> |  |   |                            |   |  |
| 14. SUBJECT TERMS<br>rock properties, nonlinear rheologies, underground explosions, seismic wave propagation, source physics   |  |   |                            | 15. NUMBER OF PAGES<br>50   |  |
|  |  |   |                            | 16. PRICE CODE  |  |
| 17. SECURITY CLASSIFICATION OF REPORT<br>Unclassified  | 18. SECURITY CLASSIFICATION OF THIS PAGE<br>Unclassified | 19. SECURITY CLASSIFICATION OF ABSTRACT<br>Unclassified | 20. LIMITATION OF ABSTRACT |   |  |

## 1. EXECUTIVE SUMMARY

### 1.1. Overview of Project

While it is generally accepted that near source nonlinearities in rock deformation influence the far-field seismic signature of a seismic source, an assessment of the importance of these nonlinearities has been hampered by a lack of well constrained rheologies with which to perform forward modeling simulations. Previous work aimed at developing nonlinear, hysteretic rheologies have largely been based on experiments covering limited stress conditions and modes of deformation. While these experiments have been important in guiding model development, the resulting models have been limited in their value due to the restricted loading paths for which they are valid.

In order to develop forward models for wave propagation in the moderate strain and damage regimes, experiments using a much wider range of loading path were needed to test and constrain models suitable for arbitrary loading paths. In this study, an experimental protocol was developed and implemented which provides detailed constraint of the nonlinear, hysteretic deformation of rock subject to arbitrary perturbations in axially symmetric compressive stresses. Experiments were performed on a diverse suite of samples, including Berea sandstone, Sierra White granite, and tuff from N-tunnel at the Nevada Test Site (NTS).

### 1.2. Project Goals

Prior to the start of this project, a rheological model had been developed for the case of uniaxial stress (see *Boitnott*, 1993). This model was thought to be illustrative of the fundamental characteristics of nonlinearities in rock deformation in the moderate strain regime, but was limited in its applicability due to the restrictive loading path for which it was valid. The underlying goal of this project was to extend this rheology to be applicable for more general loading paths.

In order to apply the developed rheology directly to problems of wave propagation from a seismic source, the rheology needed to be extended to loading paths expected in the field. To accomplish this task, four areas needed to be addressed. First, the rheology had to be extended to include a wide variety of loading conditions. In order to model compressional wave propagation (including the geometric effects of spherical wavefronts) the uniaxial-stress rheology needed to be extended to loading paths which can be transitional between uniaxial-strain and uniaxial-stress. In addition, in order to model shear wave propagation, laboratory data was needed to constrain hysteresis in the shear modulus during shear loading. Second, the effects of confining pressure on the rheological models needed to be constrained in order to address questions concerning the effect of depth of burial on the seismic signature of an underground explosion. Third, data was needed on tuff in order to make use of well calibrated field data from the Nevada Test Site. Fourth, the rheology needed to be extended into the brittle-damage regime.

### 1.3 Summary of Findings

Uniaxial stress experiments similar to those performed previously (but in this study performed as a function of confining pressure) confirmed that the uniaxial stress rheology simplifies with increasing confining pressure. Deformation becomes more

19970604 143

linear and less hysteretic with increasing confining pressure, although the observed nonlinearities clearly persist at all stress conditions studied. Complex rheological properties at reversals in loading direction (i.e.  $\Delta E$  effect, see *Boitnott*, [1993]) were found to be less evident at elevated confining pressures. As a result, the eventual rheology was simplified to make use of a common parameterization, denoted the "asymmetric bow-tie parameterization" (ABP), which appears well suited for modeling hysteresis in stress versus strain for a wide variety of loading paths. It is found that the ABP produces reasonable fits to data for all loading paths and at all stress conditions studied, provided that the stress perturbations are not exceptionally large and the loading perturbation is restricted to a single mode of deformation (see section 3).

Radial strain measured during the uniaxial stress experiments provided a test of whether a simple rheology could be constructed by assuming that the dominant source of hysteresis was in the shear component of deformation. This was found not to be the case, as the experiments indicated appreciable hysteresis (and thus energy loss) in the volumetric strain versus mean stress relationship under some conditions. Preliminary observations of radial strain during uniaxial stress perturbations lead to an initial attempt to modify of the uniaxial stress rheology to include the effects of changing confining pressure (section 2.2). While this attempt produced realistic stress-strain curves for uniaxial strain paths, the model was clearly an over-simplification as it did not hold up well when used to predict uniaxial stress data as a function of confining pressure (section 2.3). As a result, development of a rheology based on uniaxial stress and confining pressure was abandoned in favor of a different rheological description based on the decomposition of stresses into mean stress and shear stress components.

Hydrostatic stress cycling experiments confirmed that the hysteresis in the mean stress versus volumetric strain relationship was appreciable, and that it could be characterized by a qualitatively similar rheology as previously developed for the uniaxial stress versus axial strain data (i.e. can be described with an ABP for limited stress perturbations). Similarly, torsion experiments on solid cylinders were used to explore the rheology for the shear deformation. Again the rheology was found to be describable using the ABP.

The observations that the mean stress, shear stress, and uniaxial stress data could all be modeled reasonably well with the same parameterization lead to the idea that the uniaxial stress data might be modelable using a superposition of the mean stress and shear stress rheologies. However, it was found that a simple superposition was not supported by the data, as the parameters needed to fit the mean stress versus volumetric strain relationship during uniaxial stress perturbations were not quantitatively consistent with those predicted from pure mean stress experiments. Thus, the superposition was not directly generalizable to arbitrary loading paths, indicating that "coupling" had to exist between the mean stress and shear stress rheologies.

The coupling terms were clearly complex enough that it was not viable to develop a rheology based on combining results from separate experiments characterizing individual parts of the rheology. This lead to the development of a testing protocol which would have sufficient flexibility to constrain a more general rheology, including mixed mode loading paths. An experimental protocol was developed and implemented to constrain the nonlinear, hysteretic deformation of rock in the moderate strain regime. While more work is required to fully integrate the coupling terms into a

hysteretic rheology, the resulting rheology has been developed to a point where forward modeling of compressional wave propagation can be performed in order to assess which features in the rheology are important to a particular application.

Tests using loading paths which quasi-statically mimic the loading path expected from a spherically propagating compressional wave were performed to assure that the developed rheology was capable of handling explosion like loading paths. It is found that for a broad class of explosion like loading paths, a simpler rheology, using an ABP constrained from uniaxial strain data, may be sufficient for many applications.

In order to test the rheology further and explore the physical meaning of some of the parameters, tests were designed and executed which combined the static stress versus strain response with measurements of ultrasonic velocities. The velocities were used to infer the small strain dynamic moduli, and those values were compared with the moderate strain rheology. The results indicated that the moderate strain rheology does have the proper behavior in the limit of small strains, as it approaches a linear elastic model consistent with the measured velocities.

Exploratory tests were also performed on Barre granite to probe the transition into the damage regime. The experiments illustrated the added complexity of experimental characterization in the damage regime due to time dependent deformation. They also provided some indication that pressure effects on the uniaxial stress rheology are similar both within the moderate strain and damage regimes (section 5).

#### *1.4 Collaborative Efforts*

One emphasis of this project was to support other work within the AFOSR and related programs by providing laboratory data to others for the constraint of modeling efforts of near source processes and wave-propagation. Experiments performed during the course of this project were continually revised in order to better serve these projects. Projects specifically targeted for support involved: the development of an endochronic rheology for modeling wave propagation in nonlinear materials by J. B. Minster (U. Cal. San Diego) and S. Day (San Diego State Univ.); development of a damage mechanics model for wave propagation in the damage regime by C. Sammis (USC); and development of an "equivalent elastic" method for modeling wave propagation through nonlinear materials by L. Johnson (U. Cal. Berkeley ). On two occasions, students working on these projects visited NER and participated in the design, execution, and preliminary analysis of laboratory experiments.

Inna Altschul came from USC to work on tests to help characterize rock rheology in the damage regime. A number of tests were performed, and the data became a central part of her masters thesis [Altschul, 1995]. H. Xu came from U. Cal. San Diego to work on extending the endochronic rheology previously established by Day *et al.* [1993]. Specific experiments were designed to constrain the hysteretic rheology during arbitrary loading paths involving simultaneous changes in both axial and confining stresses. The results have subsequently been used for wave propagation modeling [Xu *et al.* 1996]. The data and resulting model will continue to be used as part of Xu's PhD. thesis. Experiments were also performed specifically to support Lane Johnson's development of the equivalent elastic method for modeling wave propagation (see Johnson [1996]), with the idea that laboratory data on tuff was needed to help constrain interpretation of field data from the NPE test at NTS. While the data has not yet

been used directly in this context, data on tuff from N-tunnel at NTS is now available to help constrain forward models of NTS explosions.

Other researchers also made use of the data set for the purpose of constraining models for nonlinear deformation of rocks. D. Liebllich, a PhD. student from U. Conn., was provided data to support the development of an adhesion based micromechanical model for hysteresis in rock deformation. Data was also provided to K. McCall (U. Nev. Reno) and R. Guyer (U. Mass. Amherst) for use in further development of a discrete element model for nonlinear deformation of rocks.

### *1.5 List of Publications*

The following publications resulted, either in whole or in part, from this project. Complete citations can be found in section 6.

- Altschul, I., The relationship of stress to strain in the damage regime for a brittle solid under compression, M.S. Thesis, University of Southern California, 71 pp., 1995.
- Boitnott, G. N., Experimental characterization of the nonlinear rheology of rock, PL-TR-95-2108, 1995.
- Boitnott, G. N., Constructing a general rheological model for rock deformation, PL-TR-96-2153, p. 149-158, 1996.
- Boitnott, G. N., Experimental characterization of the nonlinear rheology of rock, Int. J. Rock Mech. & Min. Sci., 34:3-4, Paper No. 033, 1997.
- Guyer, R. A., K. R. McCall, G. N. Boitnott, L. B. Hilbert Jr., and T. J. Plona, Quantitative implementation of Preisach-Mayergoyz space to find static and dynamic elastic moduli in rock, J. Geophys. Res., v. 102, n. B3, p. 5281-5293, 1997.
- Sammis, C., Stress strain modeling in the damage regime, PL-TR-95-2108, p. 491-495, 1995.
- Xu, H., S. M. Day, and J-B. H. Minster, Two-Dimensional nonlinear wave propagation in an endochronic material, PL-TR-96-2153, p. 301-308, 1996.

## 2. EXPLORATORY EXPERIMENTS

### 2.1 Overview

The first task was to design experiments which would be suitable for characterizing the rheology. As the nature of the rheology was largely unknown, a number of exploratory experiments were performed to develop baseline observations from which to identify the critical elements required for a meaningful rheology. In this section we review these experiments and provide examples of results of each type. The results are discussed in the context of how they contributed to the development of the rheological model described in section 3.

### 2.2 Initial Attempts to Extend the Uniaxial Stress Rheology

As a starting point to extend the rheology to loading conditions other than uniaxial stress, unconfined uniaxial stress experiments were performed on Sierra White granite during which both axial and radial strain were measured. These experiments were motivated by the need to identify simplifying principles which might be used to extend the uniaxial-stress rheology to the case of arbitrary (triaxial) stress perturbations.

An example of data from an experiment on Sierra White granite is shown in Figure 1. In Figure 1a we see the familiar cusped hysteresis loop between axial stress and axial strain for a cyclic axial load in unconfined compression. In Figure 1b, we plot the corresponding radial strain as a function of axial stress. Note that the radial strain exhibits little measurable hysteresis. Importantly, this observation rules out the possibility of decomposing an arbitrary deformation into a non-hysteretic dilation and hysteretic distortion, since the data indicates considerable hysteresis in the volumetric strain during perturbations in uniaxial stress.

The relative lack of hysteresis in the radial strain during unconfined compression did however indicate a possible simplifying principle which could lead to a more general rheology capable of handling loading paths transitional between uniaxial-strain and uniaxial-stress. The data in Figure 1b suggested that the radial (Poisson) expansion was a dominantly elastic phenomena. It would follow that the confining pressure required to maintain uniaxial-strain conditions should also be relatively non-hysteretic with respect to axial load. Based on this observation, we initially hoped to develop a rheological model which involved the addition of a uni-valued (non-hysteretic) dependence of the axial-strain vs. axial-stress relationship on the hydrostatic component of the stress state.

The notion that the difference between uniaxial-strain and uniaxial-stress loading may be included in the rheology with the rather simple addition of a non-hysteretic confining pressure effect was consistent with some limited observations. In Figure 2 we compare experimental data on Berea sandstone from *Hilbert et al.* [1994] with a simple extension of a rheological model previously developed for the case of unconfined compression (i.e. from *Boitnott*, [1993]). Figure 2a shows a plot of axial strain versus axial stress for uniaxial-stress and uniaxial-strain loading paths on a sample of Berea sandstone. Model predictions based on this extension of the uniaxial stress rheology are shown in Figure 2b. The model results for uniaxial-strain have been produced by adding a confining pressure effect to the uniaxial-stress model. We start by defining the axial stiffness  $\eta \equiv \partial\sigma_{11}/\partial\epsilon_{11}$ , where  $\sigma_{11}$  and  $\epsilon_{11}$  are the axial

stress and axial strain respectively. We then assume that  $\eta \equiv \lambda E$ , where  $E$  is the hysteretic Young's modulus describing the rheology for uniaxial-stress perturbations, and  $\lambda$  is a scaling factor which is a linear function of the confining stress. The confining stress is assumed to change linearly with axial stress based on the observed lack of hysteresis in the radial-strain versus axial-stress relationship as discussed in the context of Figure 1b. Note that the model results compare favorably with the experimental data, illustrating that the scaled rheology is reasonable.

### 2.3 Explicit Tests of the Effects of Confining Pressure

Explicit tests of this scaled rheology were made by performing uniaxial stress tests similar to those performed previously, but with the addition of confining pressure as a test variable. Tests were performed on Berea sandstone, Sierra White granite, and tuff from NTS.

An example of the loading protocol used on Berea Sandstone is shown in Figure 3. Stress versus strain response for two of the loading sequences are shown in Figure 4. Axial stress versus axial strain response at pressure is qualitatively similar to that observed for the unconfined tests. The same parameterization as used in *Boitnott* [1993] is found to be suitable at elevated confining pressure. As expected, the rheology does appear to simplify somewhat with pressure, with the  $\Delta E$  term getting smaller (particularly noticeable for the transition from loading to unloading) and the hysteresis loops getting stiffer, straighter, and more symmetric.

Attempts to fit the pressure effect with a simple  $\lambda$  term as described above were not very successful, particularly for Berea sandstone. Some representative plots of Young's modulus versus differential stress at various confining pressures are shown in Figures 5-7. It is clear from the data that in general,  $\lambda$  must be a function of both confining pressure and axial load. The effect of confining pressure (i.e. effective  $\lambda$ ) appears larger at low axial stress, and decreases with increasing axial stress. More problematic is the fact that  $\lambda$  for loading does not appear consistent with the required  $\lambda$  for unloading (even for a fairly restricted stress range). These discrepancies are particularly true for Berea, but also present to some extent in both the granite and tuff data. Thus the notion of  $\lambda$  as a rheological parameter was abandoned, although it still might be considered suitable in some cases as an approximate rheology (see for example section 5).

Other observations lead to the abandonment of the uniaxial stress and confining stress parameterization altogether. Unlike the data for granite discussed in section 2.2, significant hysteresis is observed between the radial strain and the axial stress for Berea and tuff, undermining the original justification for  $\lambda$  (see Figures 8b, 9b, 10b). Hysteresis between the radial strain and axial stress is also somewhat apparent in the granite at elevated confining pressures, indicating a pressure dependence of this hysteresis.

The failure of the uniaxial stress based model lead to the exploration of a rheology based on the mean stress and the shear stress (rather than the confining pressure and the differential stress). Data from experiments such as that in Figure 3 were decomposed into mean stress, shear stress, volumetric strain, and shear strain. This view of the data is plotted in Figures 8-10(c,d). This data seemed to indicate that a rheology parameterized in this way might be more flexible, and could still build on a

parameterization like that used previously for uniaxial stress. Both the mean stress and the shear stress rheologies appear rather simple, with hysteresis loop shapes mimicing the previously observed uniaxial stress behavior in many ways (note the similarity in the stress strain relationships in Figures 8-10:a,c,d). Unlike the earlier granite data, the data on Berea (and to some extent, this new data on granite as well) exhibited little hysteresis between mean stress and volumetric strain during the uniaxial stress cycles at pressure, while tuff exhibited hysteresis in this relationship (see Figure 8c, 9c, 10c). This indicated that the hysteresis observed during uniaxial stress cycles is partitioned differently for different rock types. This partitioning is also a function stress conditions and loading path for a given rock type.

#### *2.4 Mean Stress (Hydrostatic) Experiments*

The observations from the uniaxial stress tests lead to the need for some baseline measurements of the two proposed end-member rheologies; namely those for pure mean stress perturbations and pure shear stress perturbations, respectively. To begin exploring the possibility of a rheology based in part on a hysteretic bulk modulus, a set of experiments were performed to characterize the rheology describing hydrostatic stress and volumetric strain. An example loading protocol is shown in Figure 11.

Each of the samples tested exhibited considerable hysteresis in the volumetric strain versus mean stress relationship. Example stress strain curves are shown in Figures 12-14. Comparing Figures 12-14 with the mean stress plots from uniaxial stress paths in Figures 8-10, we find that the mean stress versus volumetric strain relationships are different for uniaxial stress and hydrostatic compression. For each rock-type, the pure hydrostatic cycles tend to exhibit measurably more compliant bulk moduli than observed during uniaxial stress cycles for similar mean stress variations. There also appears to be considerably more hysteresis during hydrostatic cycling than during uniaxial stress cycling (particularly for Berea sandstone and Sierra White granite) From these observations it was clear that observations of the mean stress versus volumetric strain relationship for different loading paths needed to be made in a more integrated fashion (i.e. during a single experiment) in order to constrain any systematics in the mean stress versus volumetric strain relationship for different loading paths. These experiments are discussed in section 3.

#### *2.5 Torsion Experiments*

In order to develop similar observations for shear stress behavior, torsion experiments were conducted to constrain hysteresis in the shear modulus as a function of normal load and shear stress history. Experiments were performed on hollow cylinders of intact Berea sandstone. Granite and tuff were not tested, as concurrent work indicated that other tests were more easily integrated with other data.

Examples of data on Berea sandstone are shown in Figure 15. In Figure 15a, the shear-stress vs. shear-strain relationship is plotted for a cyclic torsional load at a fixed axial load of 5.4 MPa. The frequency of the loading oscillation was 0.01 Hz and data from two different amplitude oscillations are shown. Note the nested nature of the hysteresis loops with amplitude and the fact that the mean slope of the hysteresis loops (i.e. the average shear modulus) decreases with loop amplitude. Figure 15b shows the results of three torsional oscillations at three different axial loads (3.6, 5.4, and 7.2



MPa). As expected, the average shear modulus increases, and the width of the hysteresis loops decreases, with increasing axial load.

As we might expect, the hysteresis loops appear to exhibit the same "discrete memory" and "closed-loop" characteristics as noted in studies of hysteresis in Young's modulus during uniaxial-stress perturbations. Based on this preliminary data, the hysteresis in the shear modulus appears relatively easy to model with only a few parameters. As an example, a simple "bow-tie" model for the shear modulus as a function of shear stress represents the observations fairly well (see Figure 16). In Figure 17 we plot the predicted stress-strain behavior for the experimental cases shown in Figures 15a and 15b.

Comparing these results to those from the uniaxial stress experiments, general qualitative agreement was found. Both the shear stiffening with normal load and the decreased width of the hysteresis loops are seen in the torsion and uniaxial stress data. This suggested that the shear rheology may be easily transportable between different loading paths.

### 3. CONSTRUCTING A GENERAL RHEOLOGICAL MODEL

#### 3.1 Overview

The uniaxial stress, mean stress, and torsion experiments were exploratory experiments designed to develop the necessary understanding to guide development of a realistic rheology. Based on these tests, the mean stress and shear stress were identified as good candidates for the basis of a general rheology, but it was clear that coupling terms which link shear stress effects on volumetric strain and mean stress effects on shear strain were significant enough that new experiments needed to be designed to support such a rheology.

Each of the experiments discussed in this section were performed on all three rock types, but detailed analysis of the coupling terms was restricted to data on Berea. Berea sandstone was chosen for concentrated effort because it was the most nonlinear of the three rocks being studied. In this section, we summarize the results of the experiments and discuss how they are used to develop and constrain a rheological model for nonlinear, hysteretic deformation during arbitrary loading protocols.

#### 3.2 Experimental Protocol

The loading history of an exemplary experiment is illustrated in Figure 18. The experiment involves a sequence of perturbations in load subject to varying boundary conditions and executed from a series of initial stress conditions. At three different starting stress conditions, the axial stress and confining pressure are controlled to produce perturbations in stresses enforcing the following boundary conditions: mean stress perturbations at constant differential stress (4 cycles of two different amplitudes), uniaxial stress perturbations (2 cycles), shear stress perturbations at constant mean stress (4 cycles of two different amplitudes), and uniaxial strain perturbations (4 cycles of two different amplitudes). Detail of one such sequence is shown in Figure 19.

### 3.3 Formulating a Model

The goal is to develop a model capable of predicting the stress-strain relationship for arbitrary loading paths in the stress space bounded by  $\sigma_{11} \geq \sigma_{\theta\theta}$  (i.e. axially symmetric compressive stresses). During the experiment, the strains  $\epsilon_{11}$  and  $\epsilon_{\theta\theta}$  are measured along with the stresses  $\sigma_{11}$  and  $\sigma_{\theta\theta}$ . Isotropy of deformation in the {23} plane is assumed (i.e.  $\epsilon_{\theta\theta} = \epsilon_{22} = \epsilon_{33}$ ). Each of the samples tested during the course of this work were relatively isotropic, with linear compressibilities measured in different orientations varying by less than  $\pm 5\%$ .

Intuition leads us to try to formulate a rheology in terms of the mean stress ( $\sigma$ ), the shear stress ( $\tau$ ), the volumetric strain ( $\kappa$ ), and the shear strain ( $\gamma$ ), defined as:

$$\sigma = (\sigma_{11} + 2\sigma_{\theta\theta})/3.0 \quad (1a)$$

$$\tau = (\sigma_{11} - \sigma_{\theta\theta})/2.0 \quad (1b)$$

$$\kappa = \epsilon_{11} + 2\epsilon_{\theta\theta} \quad (1c)$$

$$\gamma = \epsilon_{11} - \epsilon_{\theta\theta} \quad (1d)$$

For an isotropic, linear elastic solid,  $\kappa = \sigma/K$  and  $\gamma = \tau/G$ , where  $K$  and  $G$  are the bulk and shear moduli, respectively. Here we will generalize the definitions of the moduli to allow for the description of nonlinear, hysteretic deformation. We define the more general bulk and shear "moduli" ( $\hat{K}$  and  $\hat{G}$ ) to be:

$$\hat{K} = \frac{\partial \sigma}{\partial \kappa} \quad (2a)$$

$$\hat{G} = \frac{\partial \tau}{\partial \gamma} \quad (2b)$$

### 3.4 Pure Mode Behavior

We begin by discussing the stress versus strain relationships for perturbations in mean stress at constant shear stress and perturbations in shear stress at constant mean stress. We refer to these loading paths as "pure" mode loading paths. Over a limited but significant range in mean stress perturbations, it is found that for all rock-types the pure mode data can be modeled with a simple description of  $\hat{K}$  which will be referred to as the asymmetric bow-tie parameterization (ABP). The model parameterization, and an example comparison with data, is illustrated in Figure 20. In this model,  $\hat{K}$  is assumed to change linearly with mean stress for monotonic changes in mean stress. At any reversal in the direction of change of the mean stress,  $\hat{K}$  reverts to a value  $\hat{K}'$ , which for simplicity here is modeled as a linear function of the mean stress at the reversal in loading direction. It is also observed that the deformation exhibits a memory of the stress-strain state at previous extrema in mean stress, a characteristic commonly referred to as discrete memory (see Guyer et al. [1995]). To enforce this memory we require:

$$\int_{\sigma'}^{\sigma''} \frac{\partial \sigma}{\hat{K}_1} \equiv - \int_{\sigma''}^{\sigma'} \frac{\partial \sigma}{\hat{K}_2} \quad (3)$$

where  $\sigma'$  and  $\sigma''$  are two sequential extrema in the mean stress loading path. If we are trying to model  $\kappa$  for the loading path  $\sigma' \rightarrow \sigma'' \rightarrow \sigma'''$ , we specify (or already know)  $\hat{K}_1(\sigma)$  and use equation (3) to find  $\hat{K}_2(\sigma)$ .  $\hat{K}_2$  is then used to compute  $\kappa$  during the loading  $\sigma'' \rightarrow \sigma'''$ , and equation 3 can then be rewritten to find  $\hat{K}_3$  for the next loading leg. With prior specification of the functional form of  $\hat{K}$ , the necessary model parameters are constrained by the memory enforced by equation (3). For the case of the ABP, there are three free parameters, two describing the mean stress dependence on  $\hat{K}'$ , and one describing  $\partial\hat{K}/\partial\sigma$  during the current loading leg.

For the case of shear stress changes at constant mean stress, it is found that the same parameterization appears to describe  $\hat{G}$  (now in terms of  $\gamma$  and  $\tau$ ). Thus the ABP parameterization appears to describe the hysteresis in both the volumetric and shear strains (at constant shear and mean stress, respectively). This is found to be true for each of the rock-types tested.

Figure 21 illustrates the results of model fits to data from Berea sandstone and N-tunnel tuff. By comparing results from different initial mean stresses, it is clear that the model parameters describing  $\hat{K}$  and  $\hat{G}$  are dependent on the initial mean stress. This dependence is much stronger and functionally more complex for a rock like Berea sandstone compared to tuff. These observations illustrate that for large perturbations in  $\sigma$ , the data require a functionally more complicated parameterization, with  $\hat{K}'$  and  $\hat{G}'$  being described by nonlinear functions of  $\sigma$ . Accordingly, large amplitude perturbations also require  $\partial\hat{K}/\partial\sigma$  and  $\partial\hat{G}/\partial\tau$  during monotonic loading and/or unloading to be described by higher order functions as well (e.g. see the previous work on Young's modulus: *Boitnott* [1993]). We should also expect that  $\hat{K}$  and  $\hat{G}$  may be dependent on  $\tau$  (over and above the dependency of  $\hat{G}'$  on  $\tau$ ), and thus similar complexity should arise for large shear perturbations. Despite this complexity, over limited but rather large changes in  $\sigma$  and  $\tau$ , the ABP appears to provide a good approximation of the deformation from pure shear and pure mean stress perturbations in variety of rocks and covering a wide range of stress conditions.

### 3.5 Some Notes on Notation

Before proceeding with a discussion of the mixed mode loading paths, some notational details need to be explained. Subscripts are used to distinguish between moduli measured from different loading paths. Loading paths and their associated subscripts are as follows: mean stress ( $\sigma$ ), shear stress ( $\tau$ ), uniaxial stress ( $us$ ), and uniaxial strain ( $ue$ ). Elastic moduli inferred from compressional and shear velocities (assuming isotropy and linear elasticity) are denoted by the subscript ( $v$ ). Other common moduli are also discussed, but unlike  $\hat{K}$  and  $\hat{G}$ , are defined only for specific loading paths. These moduli include Young's modulus ( $\hat{E}_{us} \equiv \partial\sigma_{11}/\partial\epsilon_{11}|_{\Delta\sigma_{\theta\theta}=0}$ ) and the uniaxial strain modulus ( $\hat{Y}_{ue} \equiv \partial\sigma_{11}/\partial\epsilon_{11}|_{\Delta\epsilon_{\theta\theta}=0}$ ). In similar fashion, a generalized Poisson's ratio ( $\nu_{us} \equiv -\partial\epsilon_{\theta\theta}/\partial\epsilon_{11}|_{\Delta\sigma_{\theta\theta}=0}$ ) is also used. Parameters denoted without the ( $\hat{\cdot}$ ) represent values inferred from other parameters assuming isotropic, linear elasticity (e.g.  $E_{\sigma\tau}$  is the inferred Young's modulus derived from measurements of  $\hat{K}_{\sigma}$  and  $\hat{G}_{\tau}$ ). The superscript ( $'$ ) is used to denote the value of a parameter measured immediately after a reversal and loading direction, and symbols enveloped in  $\langle \rangle$  denote the average value

of the enveloped parameter over an extended range of loads (such as over an entire loading and unloading cycle).

### 3.6 Behavior During Mixed Mode Loading Paths

Unfortunately, the data indicate that, in general, it is not sufficient to superimpose the rheologies discussed above for  $\hat{K}_\sigma$  and  $\hat{G}_\tau$  to describe deformation during arbitrary (mixed-mode) loading paths. While under some conditions, and for some rock types, a simple decoupled model may be appropriate, additional effects are commonly observed. Figures 22a, 23a and 24a plot the volumetric strain as a function of the mean stress for Berea sandstone, NTS tuff, and Sierra White granite during the 2nd perturbation sequence (as shown in Figures 18 and 19). Here we see that for the mixed mode cases (i.e. uniaxial stress and uniaxial strain),  $\hat{K}_\sigma$  is not sufficient to model the volumetric strain during other modes of deformation.

We do however note some pattern to the stress-strain behavior shown in Figures 22a, 23a, and 24a. In those figures, it can be seen that the shear stress perturbation (at constant mean stress) causes an appreciable decrease in volumetric strain (i.e. a dilation). Accordingly, the uniaxial-stress and uniaxial-strain perturbations produce less volumetric strain (per unit change in mean stress) than is observed during the pure mean stress cycles. This suggests that a "coupling" term is required to handle volumetric strain resulting from changes in shear-stress. Similarly for the shear strain (Figures 22b, 23b, and 24b), there is again evidence of coupling in the sense that the shear stress versus shear strain relationship is not fully described by  $\hat{G}_\tau$  when  $\sigma$  is changing. Here again, a coupling term is required to handle the effects of mean stress changes on the shear rheology.

### 3.7 Characterizing the Coupling Terms

The coupling terms appear to be a strong function of rock type, and for Berea appear to become less significant as the initial mean stress increases. It is likely that they result at least in part from stress induced anisotropy in mechanical properties in response to differential loads.

In many respects, the coupling terms appear relatively elastic (i.e. uni-valued functions of stress state), allowing for the potential to develop a general rheology by superposition of elastic coupling terms with hysteretic and stress dependent  $\hat{K}_\sigma$  and  $\hat{G}_\tau$ . The development of a hysteretic rheology is not fully completed. In its place, a nonlinear elastic (non-hysteretic) approximation to the data is developed here, which will prove useful as an illustration of the general character of the coupling terms. The rheology can be described by:

$$\Delta\kappa = \frac{\Delta\sigma}{\hat{K}_\sigma} + \Delta\tau \cdot \zeta(\sigma, \tau) \quad (4a)$$

$$\Delta\gamma = \frac{\Delta\tau}{\hat{G}_\tau} + \Delta\sigma \cdot \psi(\sigma, \tau) \quad (4b)$$

The terms  $\zeta$  and  $\psi$  are the coupling terms.  $\zeta$  handles the effects of changing shear stress on the mean stress rheology and  $\psi$  handles the effects of changing mean stress on the shear rheology.

While the form of the coupling terms is still not fully developed, reasonable behavior can be achieved using functionally similar forms for  $\zeta$  and  $\psi$ :

$$\zeta = -A \tau^\alpha e^{-a\sigma} \quad (4c)$$

$$\psi = -B \tau^\beta e^{-b\sigma} \quad (4d)$$

Preliminary attempts to fit the Berea sandstone data lead to the following values:  $\langle A \rangle \approx 1.8e-05 \text{ MPa}^{-(\alpha+1)}$ ,  $\langle \alpha \rangle \approx 1.5$ ,  $\langle a \rangle \approx 0.2 \text{ MPa}^{-1}$ ,  $\langle B \rangle \approx 8.0e-06 \text{ MPa}^{-(\beta+1)}$ ,  $\langle \beta \rangle \approx 1.0$ , and  $\langle b \rangle \approx 0.05 \text{ MPa}^{-1}$ . Using these values, along with constant values of  $\langle \hat{K}_\sigma \rangle = 10 \text{ GPa}$  and  $\langle \hat{G}_\tau \rangle = 8 \text{ GPa}$ , model predictions for the data in Figure 22 is shown in Figure 25. Note that the nonlinear model (equations 4a-d) reproduces the dominant features in the data, with the exception of the hysteresis which in this case has been explicitly ignored.

One underlying implication of the coupling terms is that inferred (average) elastic moduli are a function of the loading path and the stress state from which they are derived. As an illustration, equations 4a and 4b can be rewritten as:

$$\hat{K} = \frac{\hat{K}_\sigma}{1 + r \hat{K}_\sigma \zeta} \quad (5a)$$

$$\hat{G} = \frac{r \hat{G}_\tau}{r + \hat{G}_\tau \psi} \quad (5b)$$

where  $r$  is the stress trajectory parameter ( $r = \Delta\tau/\Delta\sigma$ ). Note that if  $r$  is positive,  $\hat{K} > \hat{K}_\sigma$  and  $\hat{G} > \hat{G}_\tau$  (since  $\zeta$  and  $\psi$  are found to be negative).

### 3.8 Comparisons with dynamic moduli

The coupling terms described by equations 4c and 4d have been derived from moderate stress amplitude perturbations, and it remains unclear as to whether they result from stress hysteretic phenomenon or if they are dominantly elastic in character. To begin addressing this issue a second testing protocol was developed which combines a complex loading history, static strain measurements, and ultrasonic velocity measurements. Compressional and shear velocities were measured using ultrasonic pulse propagation ( $\approx 1 \text{ MHz}$ ) along the axis of the cores. As in the previous experiments, room dry Berea sandstone was used as the sample material. The addition of the velocity data provides information concerning the mechanical properties (i.e. moduli) for very small stress perturbations, and thus should provide constraints on the behavior of  $\zeta$  and  $\psi$  in the limit of small strains.

The loading protocol is shown in Figure 26. After an initial loading and unloading of the confining pressure (to season the sample), confining pressure was increased to 50 MPa and velocities were measured at 5 points during the loading. The confining pressure was returned to 5 MPa, and a slight differential load (1 MPa) was applied. Confining pressure was then increased (at constant differential stress), stopping at the same 5 points for which velocities were measured during hydrostatic loading. At each of these 5 points during the loading, a series of stress perturbations was applied, consisting of perturbations in mean stress, uniaxial stress, and shear stress. Velocities were measured at various points during this loading sequence.

The observed nonlinearities in the static stress-strain relationships are quantitatively consistent with those from the moderate strain experiments discussed earlier. Stress-strain relationships during the mean stress and shear stress perturbations are used to infer  $\langle \hat{K}_\sigma \rangle$  and  $\langle \hat{G}_\tau \rangle$ . Stress-strain relationships during the uniaxial stress perturbations are used to infer Young's modulus and Poisson's ratio ( $\langle \hat{E}_{us} \rangle$  and  $\langle \hat{\nu}_{us} \rangle$ ). In addition, velocities measured during the hydrostatic loading (events 1-5 in Figure 26) are used, along with the measured bulk density, to infer dynamic elastic constants controlling compressional and shear velocities ( $Y_v$  and  $G_v$ ). Assuming isotropic, linear elasticity, these three sets of elastic constants were used to compute (infer) all other elastic constants. Thus there are three sets of inferred elastic constants, one inferred from pure mode perturbations, the second inferred from the mixed mode perturbation of uniaxial stress, and the third inferred from the compressional and shear velocities.

The inferred moduli are plotted in Figure 27. Comparing the results of the two static measurements, the expected systematic differences between elastic constants inferred using pure modes and those inferred from uniaxial stress are clearly seen. Most notably, inferred bulk modulus is higher for uniaxial stress than it is for the mean stress perturbation. This is the result of finite  $\Delta\tau \cdot \zeta$  during the uniaxial stress perturbations. Inferred shear modulus is not notably different for the two cases, as is predicted by the nonlinear rheology for these stress conditions.

Comparing these results with the moduli derived from the velocities, the statically determined moduli are in general lower. Importantly, the systematics between the  $K$ 's and  $G$ 's with respect to the mean stress are similar between the pure mode static and the velocity derived cases, and different for the mixed mode static case (uniaxial stress). This difference in systematics with mean stress is clearly reflected in the estimates of the  $\nu$ 's, which for isotropic, linear elasticity, is sensitive only to the ratio  $K/G$ .

### 3.9 Correcting for Strain Amplitude

It has long been realized that the stress amplitude of the perturbations used to measure elastic constants strongly influences the measured values, and that this is one of the dominant causes of discrepancies between small amplitude dynamic measurements and larger amplitude static measurements (see for example Walsh, [1965]). Stress amplitude effects arise primarily from hysteretic nonlinearities. In the limit of small strains, hysteresis is minimized and it is found that inferred moduli (for a particular mode of deformation) approach the moduli at reversals in load observed during larger amplitude cycles (see Guyer *et al.* [1997]). In order to better compare the static

and dynamic data collected here, the local moduli  $\hat{K}'_{\sigma}$ ,  $\hat{G}'_{\tau}$ ,  $\hat{E}'_{us}$ , and  $\hat{\nu}'_{us}$  at each reversal in loading direction were used in place of  $\langle \hat{K} \rangle$ ,  $\langle \hat{G} \rangle$ ,  $\langle \hat{E}_{us} \rangle$ , and  $\langle \hat{\nu}_{us} \rangle$ . These stress amplitude corrected moduli were then compared with the dynamic moduli from the ultrasonic velocities. Results are plotted in Figure 28. The strain amplitude correction of the static moduli results in an elevation of the moduli with respect to their predecessors (i.e. static values in Figures 27a and 27b). Importantly, the amplitude correction has not changed the systematics between the  $K$ 's,  $G$ 's, and  $\nu$ 's with mean stress for either case.  $\hat{K}'_{\sigma}$  and  $\hat{G}'_{\tau}$  from pure mode static measurements, compare favorably with  $K_v$  and  $G_v$  from the velocities, although velocity derived moduli are still slightly higher.  $G'_{us}$  is not significantly different from  $\hat{G}'_{\tau}$ , but  $K'_{us}$  is notably higher than the inferences  $\hat{K}'_{\sigma}$ .

### 3.10 Some General Remarks About the Rheology

The experiments clearly demonstrate that the deformation of all of the samples tested is nonlinear. The data, along with a nonlinear elastic model which approximates much of the observed nonlinearity, illustrate that elastic moduli are dependent on the mode of deformation from which they have been measured. The most dominant coupling effect in Berea sandstone is the  $\zeta$  term, which acts to increase the bulk modulus ( $\hat{K}$ ) during mixed mode loading paths where both mean stress and shear stress increase (or decrease) simultaneously.

The magnitude of the coupling terms  $\zeta$  and  $\psi$  are found to decrease with increasing mean stress, and increase with increasing shear stress. They likely reflect, at least in part, shear stress (i.e. differential stress) induced anisotropy. As differential stress is increased, the stiffness to axial deformation is increased, thus resisting both volumetric and shear strains. In addition, the coupling terms may also reflect shear stress induced dilatancy, as grain and crack surfaces attempt to slide past opposing features.

There is some limited evidence that the stress induced anisotropy mechanism is the dominant process, as the coupling terms controlling moderate stress amplitude moduli (e.g.  $\langle \hat{K} \rangle$  and  $\langle \hat{G} \rangle$ ) also appear to control strain amplitude corrected moduli (e.g.  $\hat{K}'$  and  $\hat{G}'$ ). Evidence of shear induced dilatancy is less clear, but is appealing in that dilatancy is known to occur at higher differential stresses. It is interesting to note that the nonlinear rheology presented in equations 4a-d predicts dilatancy (i.e.  $\hat{K} < 0.0$ ) at high differential stresses. While extension to higher differential stresses will require higher order functions for  $\zeta$  and  $\psi$  (as well as hysteresis in these terms), it is reasonable to expect that the rheology is extendible to these conditions.

Development of a hysteretic rheology which includes all of the observed effects of loading path still requires more work. Reasonable behavior can be attained by using hysteretic pure mode moduli ( $\hat{K}_{\sigma}$  and  $\hat{G}_{\tau}$ ) and combining them with nonhysteretic coupling terms (i.e. placing hysteretic  $\hat{K}_{\sigma}$  and  $\hat{G}_{\tau}$  in equations 4a,b). The model does not produce the observed reduction in hysteresis of  $\hat{K}$  during uniaxial stress cycles and also tends to over-predict hysteresis in  $\hat{G}$  during mixed mode loading. In the context of the rheology developed here, these effects require either the introduction of hysteretic coupling terms or the replacement of  $\hat{K}_{\sigma}$  and  $\hat{G}_{\tau}$  in equations 4a,b with loading path dependent terms. It should also be noted that the coupling terms described here could easily be introduced into the endochronic rheology of Xu *et al.* [1996]. Their

endochronic rheology is essentially nothing more than a simple decoupled superposition of  $\hat{K}_\sigma$  and  $\hat{G}_\tau$  (using a different parameterization than developed here), and thus adding elastic coupling terms should be straightforward. Despite the shortcomings of the use of nonhysteretic coupling terms, the resulting rheology mimics observation remarkably well, and thus should be suitable to assess whether the observed nonlinearities are important in the context of a particular application.

## 4. THE EXPLOSION LOADING PATH

### 4.1 A Simpler Rheology for an Important Loading Path

Despite the apparent complexity introduced by the coupling terms, we find that a related but simpler rheology can be formulated which is applicable to the case of compressional wave propagation from an explosive source. Figure 29 illustrates the loading protocol of an experiment designed to characterize deformation during loading paths which mimic (quasi-statically) the stress path expected as a result of an underground explosion. The loading paths are constructed to follow that predicted for a Heaviside step function in radial stress at a spherical cavity in a linear elastic material. The resulting explosion loading path involves a uniaxial strain loading followed by a mixed-mode unloading which follows a damped oscillation about a final stress state. The unloading path is a function of the range (distance from source) and the effective elastic constants of the material. In the experiment illustrated in Figure 29, we have performed four cycles of uniaxial strain loading, followed by three successive explosion loading paths with increasing amplitude (representing decreasing range).

Figure 30 illustrates the stress-strain relationship during this experiment, deconvolved into stresses and strains as defined in equations 1[a,b,c,d]. Here we see that the deformation is well behaved (although nonlinear and hysteretic), without noticeable complications by the coupling terms (as was seen in Figure 22). In fact, the data can be modeled fairly well using a uncoupled ABP for both  $\hat{K}_{u\epsilon}$  and  $\hat{G}_{u\epsilon}$ , (i.e. where  $\hat{K}$  and  $\hat{G}$  are constrained by the uniaxial strain data). Note how the loops for the explosion paths are not easily distinguishable from the uniaxial strain loops which preceded them. In effect, this short-cut groups the coupling terms discussed previously into the ABP description of  $\hat{K}_{u\epsilon}$  and  $\hat{G}_{u\epsilon}$ , and is thus valid only for loading paths for which the coupling terms themselves are functionally consistent with the ABP. The explosion loading path examined here appears to be such a path, and thus this simplified model appears appropriate for the problem of the spherically propagating compressional wave for an explosion-like source.

Figure 31 illustrates the stress-strain relationship for N-Tunnel tuff during an experiment of the type illustrated in Figure 29. Again, the deformation (both volumetric and shear) for the explosion loading path is found to be modelable using an "uncoupled" rheology constrained by the uniaxial strain path.

In Figure 32, we compare the measured strain paths with the strain paths predicted by a linear elastic rheology (for the identical stress paths) for two explosion paths in Berea Sandstone. The elastic constants used for the linear elastic predictions are constrained to enforce the uniaxial strain loading leg during the early stages of the loading path. The measured strain path upon unloading is noticeably different from that of the linear elastic model. Such differences are readily noted even for conditions



which would typically be considered well outside the elastic radius.

The implications of these differences are not well known at this point. However, qualitatively one can reason that if the measured strains were used to infer a stress path (using a linear elastic model), the inferred stress path would be different from the actual stress path. Thus, if back-propagated to the source, the error would result in an incorrect (unphysical) source function. In addition to this contamination of an observation at a particular range, the rheology will also have effects on the propagation of the compressional wave itself, further distorting a source function derived through inappropriate use of a linear elastic model.

#### *4.2 Observations at Larger Stress Amplitudes*

A few exploratory tests have been performed in an attempt to see when the character of the deformation changes as we go to higher stress amplitudes. At an initial mean stress of 10 MPa, an experiment on Berea sandstone (Figure 33) with peak axial stresses of 80 MPa illustrates that the same rheology appears to hold even for these large strains. A experiment on N-Tunnel tuff behaved similarly for peak axial stresses of 40 MPa, but caused failure during the uniaxial strain loading during an attempt to go to 80 MPa. These experiments indicate that the rheology appears viable over the entire moderate strain regime (until the onset of damage).

In the small strain limit, the rheology approaches a non-linear elastic model at low mean stresses and a linear elastic model at high ambient mean stresses. In previous work, the rheology has been shown to remain viable to strain amplitudes as low as  $10^{-5}$ .

### **5. CONFINED COMPRESSION AND DAMAGE**

Experiments have also been conducted on Barre granite as exploratory experiments for studying the effect of confining pressure on uniaxial stress deformation and for extending the moderate strain regime rheology into the brittle damage regime. Figure 34 illustrates an example of the stress history of one of the experiments. Experiments have been performed at two different confining pressures (0 MPa and 10 MPa respectively).

Stress-strain results are shown in Figure 35a. During the loading, numerous small perturbations in the load were imposed to measure the unloading stiffness. In these experiments we find that once we enter the damage regime (i.e. differential stress levels above 150 MPa), the stress-strain relationship during cyclic loading exhibits a ratcheting effect, which becomes more pronounced as we approach failure. This ratcheting is thought to reflect time dependent crack growth, but may also include static (rate independent) phenomena as well.

The data provides some preliminary constraint on confining pressure effects in the moderate-strain and damage regimes. In Figure 35b, The logarithm of the local Young's modulus ( $E$ ) during loading for each experiment is plotted using solid lines and the logarithm of the unloading stiffnesses ( $E'$ ) are plotted using circles. Looking at the data in the moderate-strain regime (differential stresses below 150 MPa), we see that

the effect of confining pressure on both  $E$  and  $E'$  can be modeled with a simple scale factor which is of comparable magnitude for both  $E$  and  $E'$ . This is consistent with the  $\lambda$  parameter as discussed earlier. As discussed in the context of the uniaxial stress data in section 2, the data here indicates that  $\lambda$  is a function of differential stress at low axial loads. Also note that once in the brittle-damage regime, this simple scaling with confining pressure breaks down, as the effect of confining pressure on  $E$  develops a more pronounced pressure effect than on  $E'$ , which is likely due in large part to time dependent damage and resulting deformation.

## 6. REFERENCES

- Altschul, I., The relationship of stress to strain in the damage regime for a brittle solid under compression, M.S. Thesis, University of Southern California, 71 pp., 1995.
- Boitnott, G. N., Fundamental observations concerning hysteresis in the deformation of intact and jointed rock with applications to nonlinear attenuation in the near source region, *in* Proceedings of the Numerical Modeling for Underground Test Monitoring Symposium, Durango, Colorado, LA-UR-93-3839, p.121-134, 1993.
- Boitnott, G. N., Experimental characterization of the nonlinear rheology of rock, PL-TR-95-2108, *in* Proceedings of the 17th Seismic Research Symposium on Monitoring a Comprehensive Nuclear Test Ban Treaty, 12-15 Sept., 1995.
- Boitnott, G. N., Constructing a general rheological model for rock deformation, *in* Proceedings of the 18th Annual Seismic Research Symposium on Monitoring a Comprehensive Test Ban Treaty, 4-6 September, PL-TR-96-2153, p. 149-158, 1996.
- Boitnott, G. N., Experimental characterization of the nonlinear rheology of rock, *Int. J. Rock Mech. & Min. Sci.*, 34:3-4, Paper No. 033, 1997.
- Day, S., J-B. Minster, M. Tryon, and L. Yu, Nonlinear hysteresis in an endochronic solid, *in* Proceedings of the Numerical Modeling for Underground Test Monitoring Symposium, Durango, Colorado, LA-UR-93-3839, p.135-148, 1993.
- Guyer, R. A., K. R. McCall, and G. N. Boitnott, Hysteresis, discrete memory, and nonlinear wave propagation in rock: a new paradigm, *Phys. Rev. Lett.*, v. 74, p. 3491, 1995.
- Guyer, R. A., K. R. McCall, G. N. Boitnott, L. B. Hilbert Jr., and T. J. Plona, Quantitative implementation of Preisach-Mayergoyz space to find static and dynamic elastic moduli in rock, *J. Geophys. Res.*, v. 102, n. B3, p. 5281-5293, 1997.
- Hilbert, L. B., T. Hwong, N. Cook, K. Kihei, and L. Myer, Effects of Strain Amplitude on the Static and Dynamic Nonlinear Deformation of Berea Sandstone, *in* Rock Mechanics Models and Measurements Challenges from Industry, Proc. 1st N. Amer. Rock Mech. Symp., A.A. Balkema, 1994.
- Johnson, L. The effect of damage on explosion generated elastic waves, *in* Proceedings of the 18th Annual Seismic Research Symposium on Monitoring a Comprehensive Test Ban Treaty, 4-6 September, PL-TR-96-2153, p. 195-198, 1996.
- Sammis, C., Stress strain modeling in the damage regime, *in* Proceedings of the 17th Seismic Research Symposium on Monitoring a Comprehensive Nuclear Test Ban

Treaty, 12-15 Sept., PL-TR-95-2108, p. 491-495, 1995.

Walsh, J. B., The effect of cracks on the uniaxial elastic compression of rocks, J. Geophys. Res., v. 70, n. 2, pp. 399-411, 1965.

Xu, H., S. M. Day, and J-B. H. Minster, Two-Dimensional nonlinear wave propagation in an endochronic material, in Proceedings of the 18th Annual Seismic Research Symposium on Monitoring a Comprehensive Test Ban Treaty, 4-6 September, PL-TR-96-2153, p. 301-308, 1996.

### Sierra White Granite

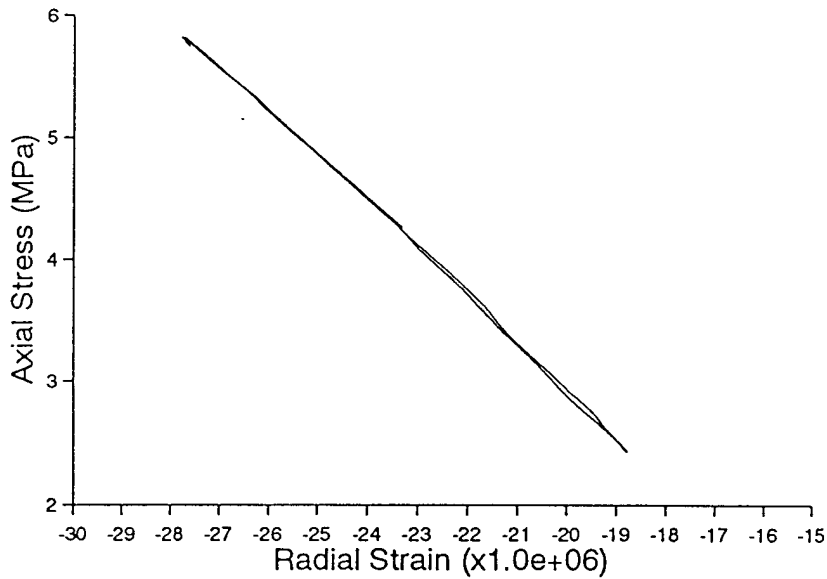
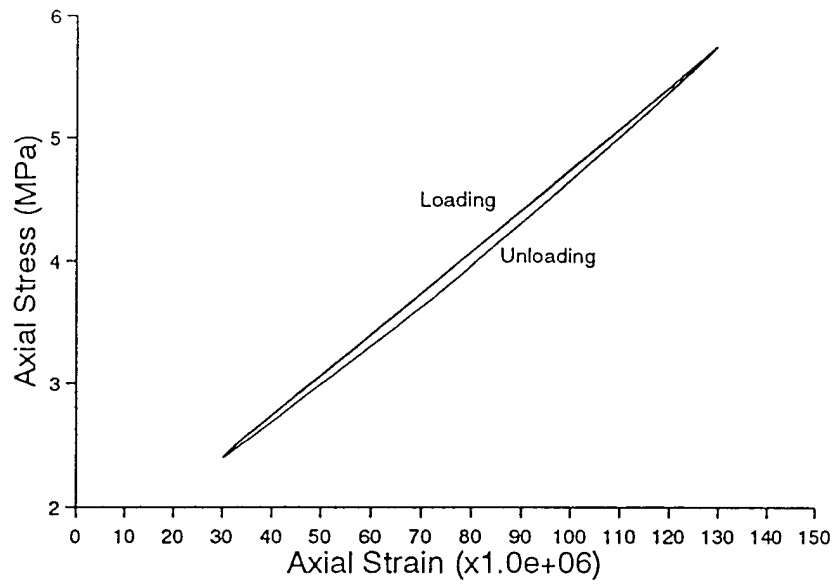


Figure 1: Axial stress versus axial strain and axial stress versus radial strain for cyclic loading of Sierra White granite in unconfined compression. Note the absence of hysteresis in the radial strain. This observation allows for the possibility of a simple model incorporating the effects of confining pressure on the hysteresis in axial strain.

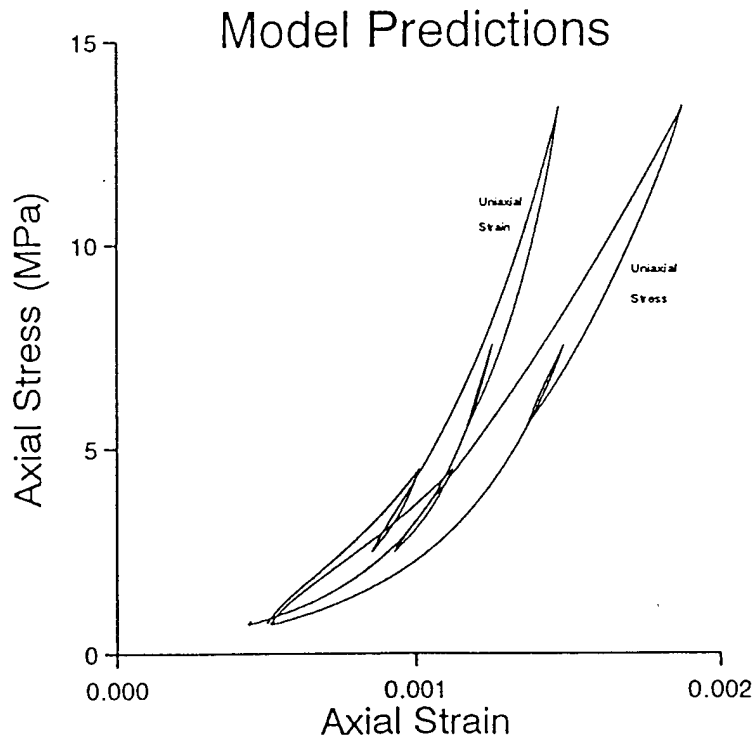
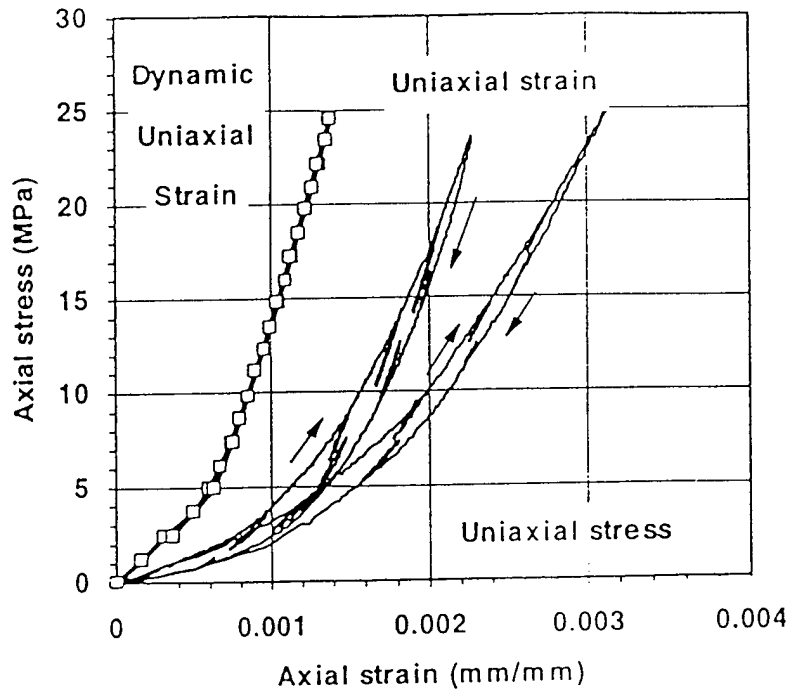


Figure 2: Comparison of Experimental data (from *Hilbert et al.*, 1994) with model predictions for hysteretic deformation in Berea Sandstone. A simple scaling law is used to incorporate the effects of changing confining pressure on the axial stiffness during uniaxial strain loading. The simple model appears to contain many of the features exhibited by the data. Model results are based on experiments using a different sample of Berea sandstone, and thus small quantitative discrepancies between model and data should not to be considered significant.

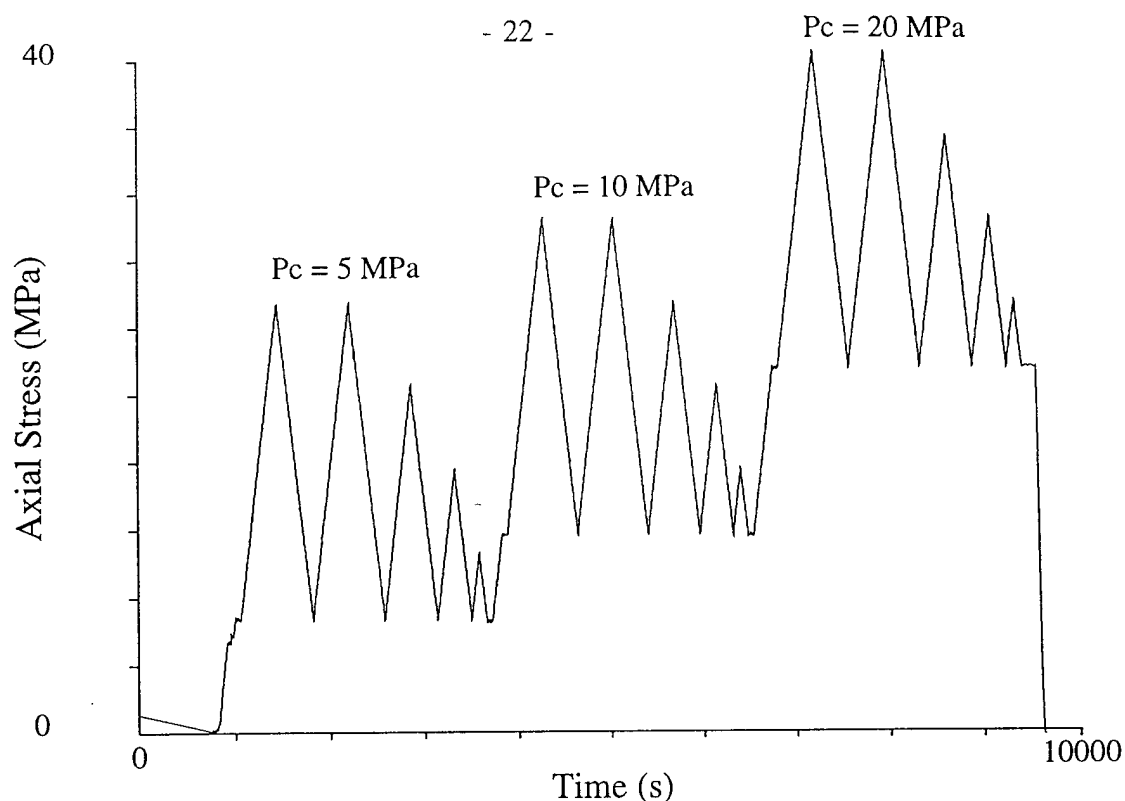


Figure 3: Example of the loading protocol used to constrain the effect of confining pressure on the uniaxial stress rheology. At a series of different confining pressures ( $P_c = 5, 10$ , and  $20$  MPa) A sequence of axial stress perturbations were made while axial and radial strain were monitored.

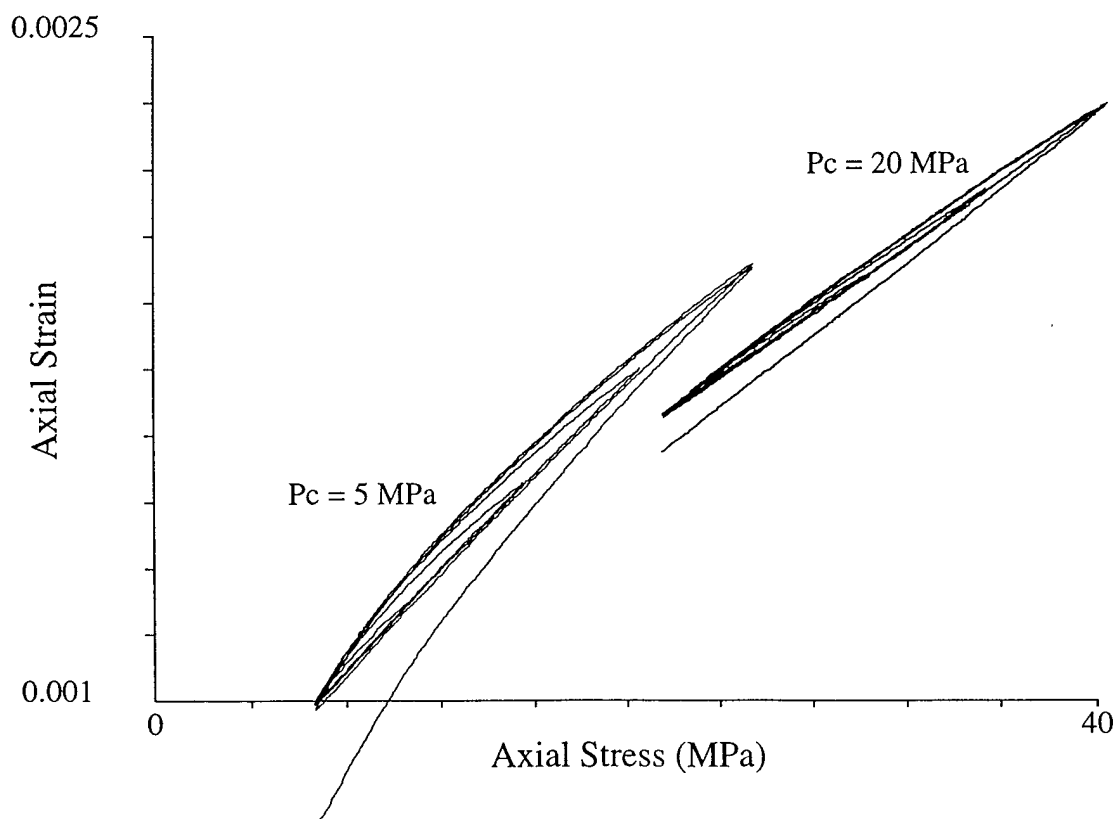


Figure 4: Axial stress versus axial strain for Berea sandstone during the axial loading sequences at  $5$  and  $20$  MPa confining pressure shown in figure 3.

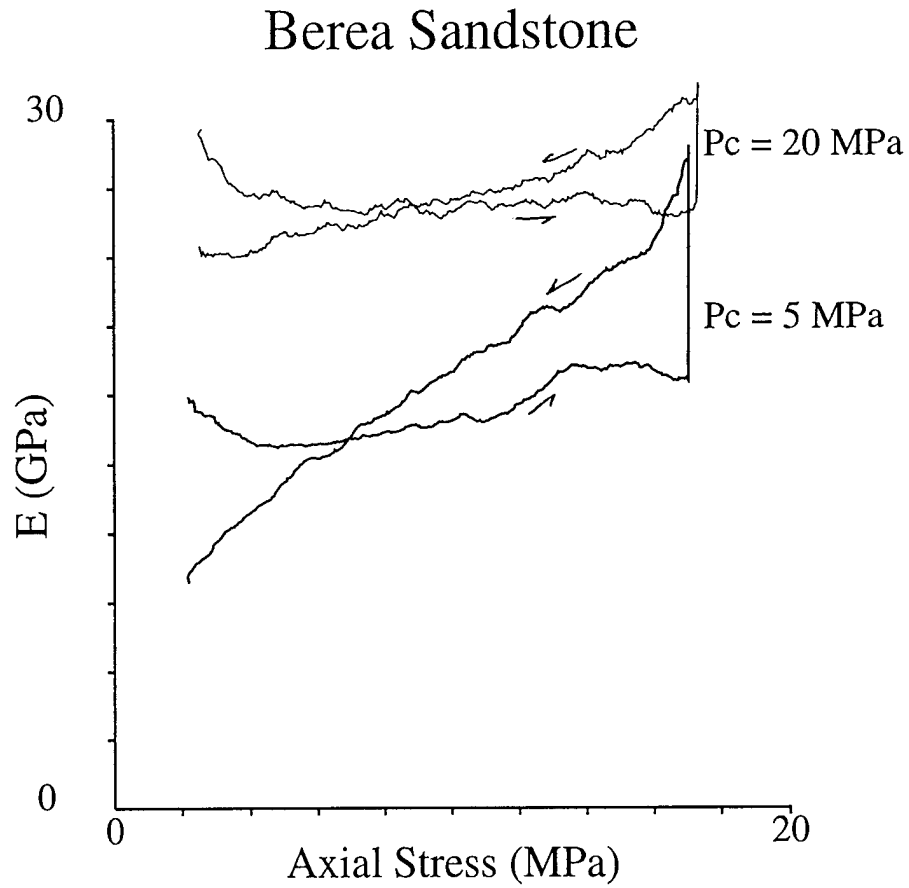


Figure 5: Local Young's modulus ( $E = \partial\sigma_{11}/\partial\epsilon_{11}$ ) for Berea sandstone during uniaxial stress cycles at 5 and 20 MPa confining pressure. Data is from the second large amplitude stress cycle at each pressure in the sequence shown in Figure 3. Arrows indicate loading direction.

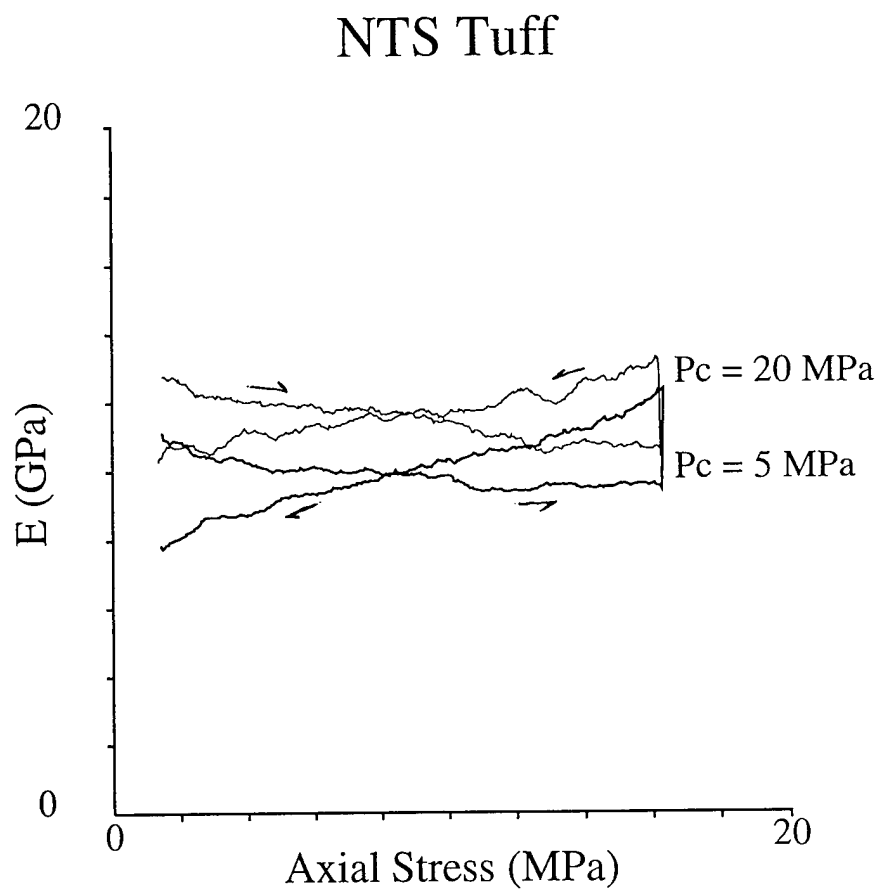


Figure 6: Local Young's modulus ( $E = \partial\sigma_{11}/\partial\epsilon_{11}$ ) for N-Tunnel tuff during uniaxial stress cycles at 5 and 20 MPa confining pressure. Data is from the second large amplitude stress cycle at each pressure in the sequence similar to that shown in Figure 3. Arrows indicate loading direction.



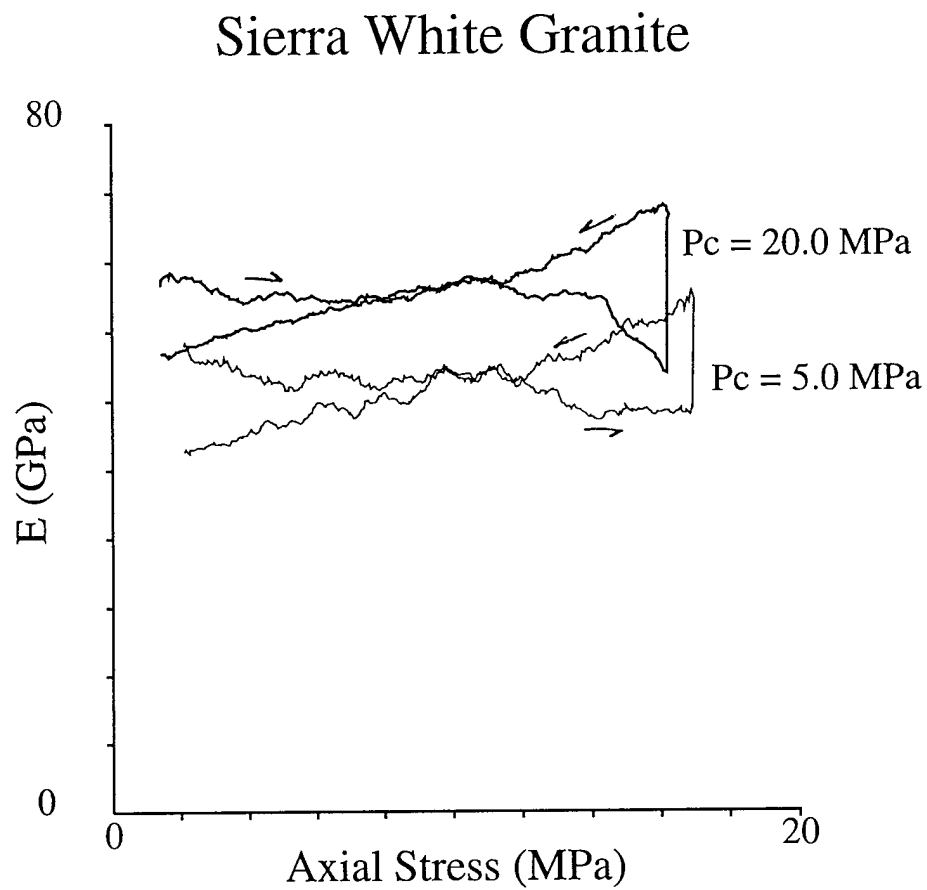


Figure 7: Local Young's modulus ( $E = \partial\sigma_{11}/\partial\epsilon_{11}$ ) for Sierra White granite during uniaxial stress cycles at 5 and 20 MPa confining pressure. Data is from the second large amplitude stress cycle at each pressure in the sequence similar to that shown in Figure 3. Arrows indicate loading direction.

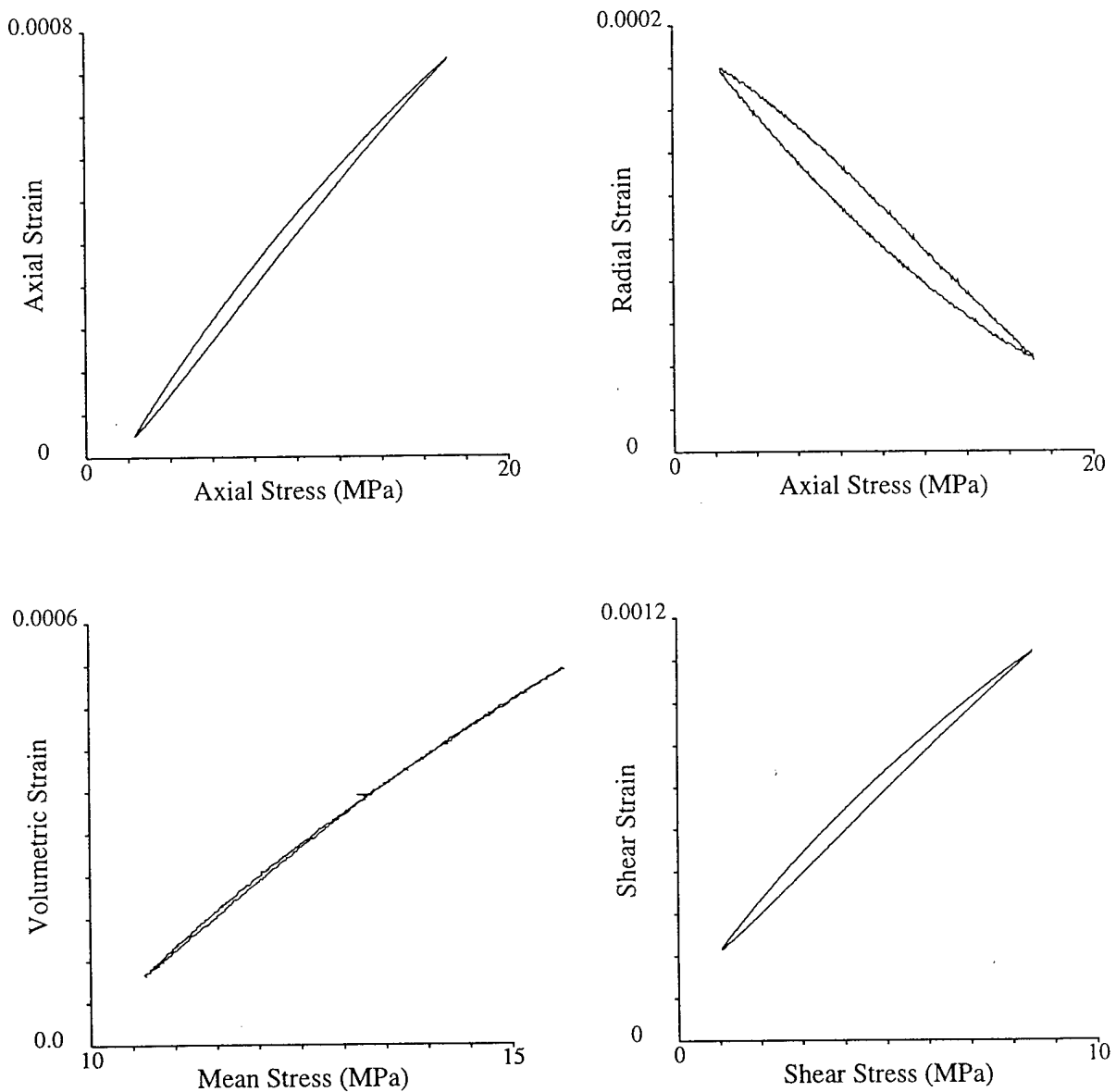


Figure 8: Stress versus strain for Berea sandstone during a uniaxial stress cycle at a confining pressure of 10 MPa. a) Axial stress versus axial strain. b) Radial stress versus radial strain. c) Mean stress versus volumetric strain. d) Shear stress versus shear strain. Note the strong hysteresis in (b) and the lack of hysteresis in (c). In this case the hysteresis can be thought to be confined to the shear rheology.

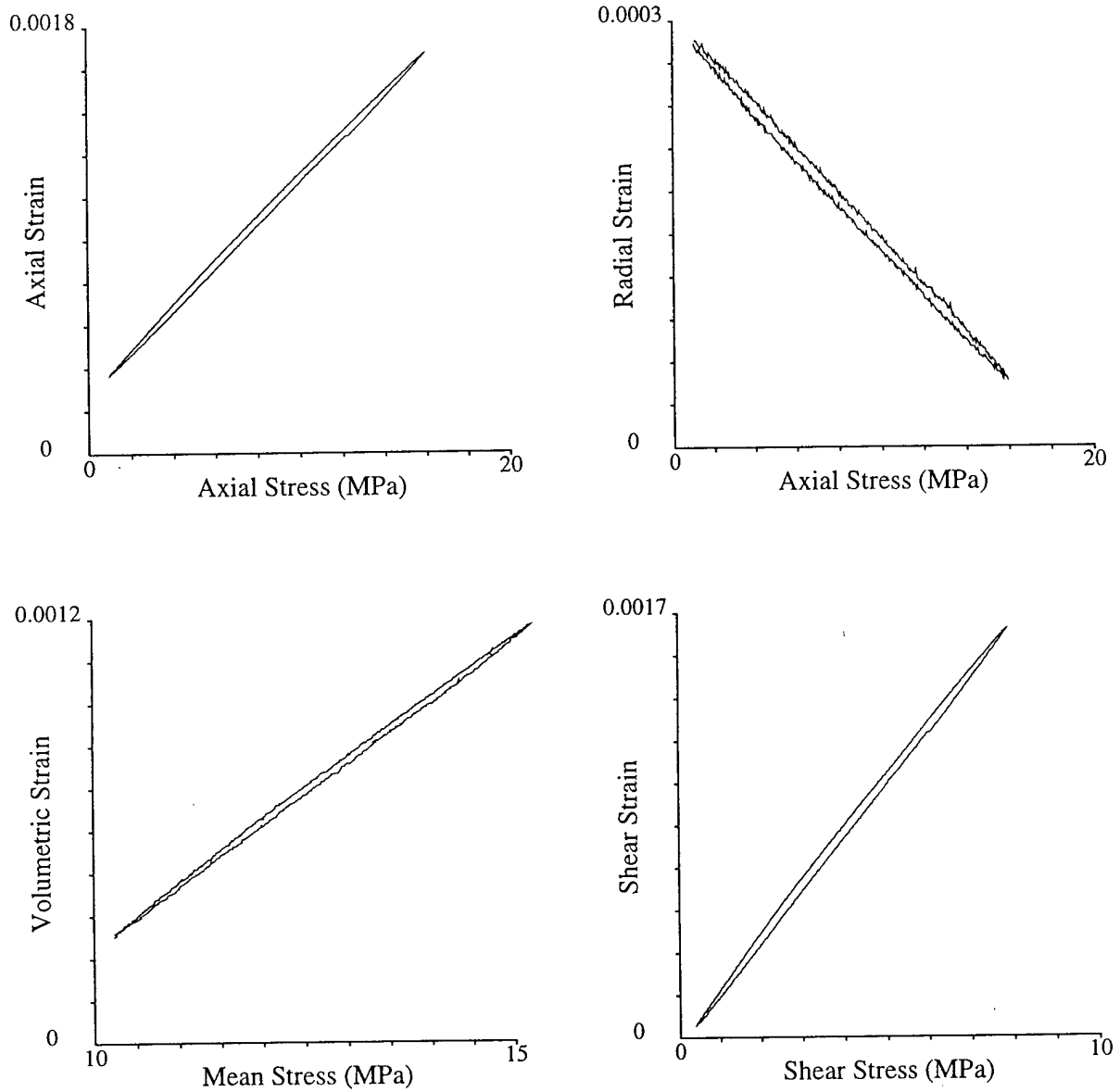


Figure 9: Stress versus strain for N-Tunnel tuff during a uniaxial stress cycle at a confining pressure of 10 MPa. a) Axial stress versus axial strain. b) Radial stress versus radial strain. c) Mean stress versus volumetric strain. d) Shear stress versus shear strain. Note the measurable hysteresis in each plot, indicating that both the mean stress and the shear stress rheologies are hysteretic.

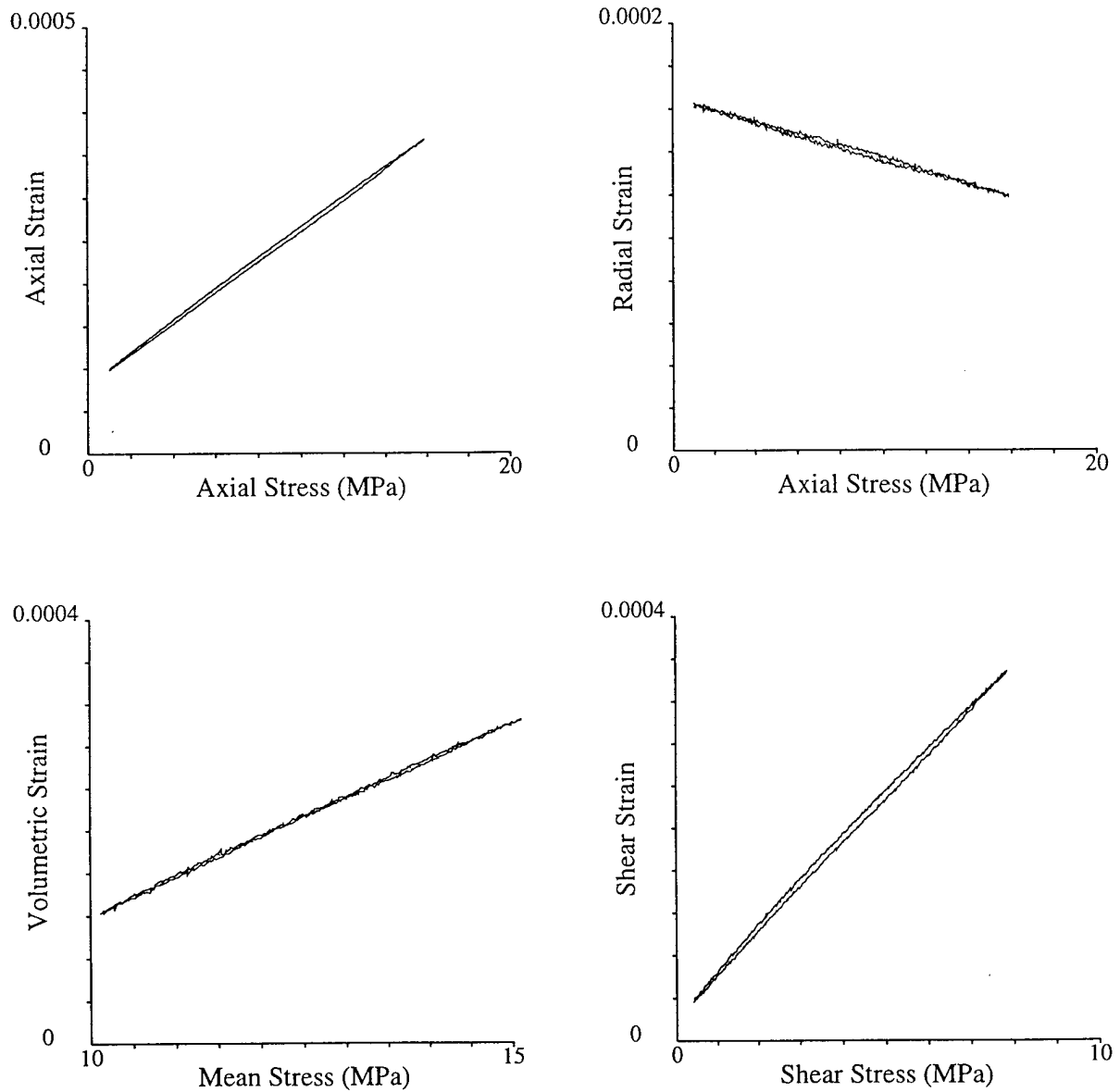


Figure 10: Stress versus strain for Sierra White granite during a uniaxial stress cycle at a confining pressure of 10 MPa. a) Axial stress versus axial strain. b) Radial stress versus radial strain. c) Mean stress versus volumetric strain. d) Shear stress versus shear strain. Note the measurable hysteresis in (b) which was not observed during the unconfined test in figure 1.

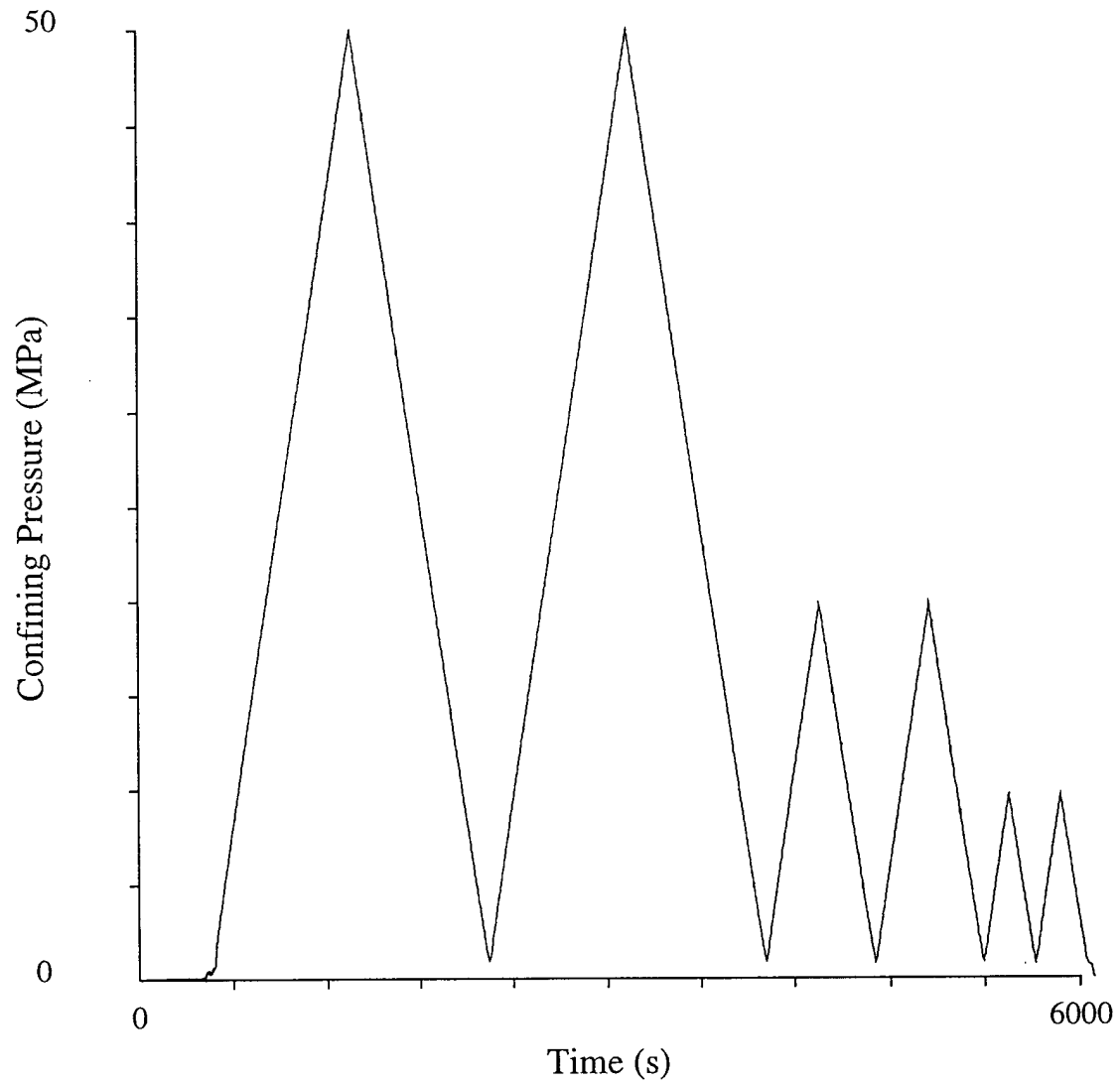


Figure 11: Loading protocol used to characterize the hysteretic deformation resulting from hydrostatic stress cycling.

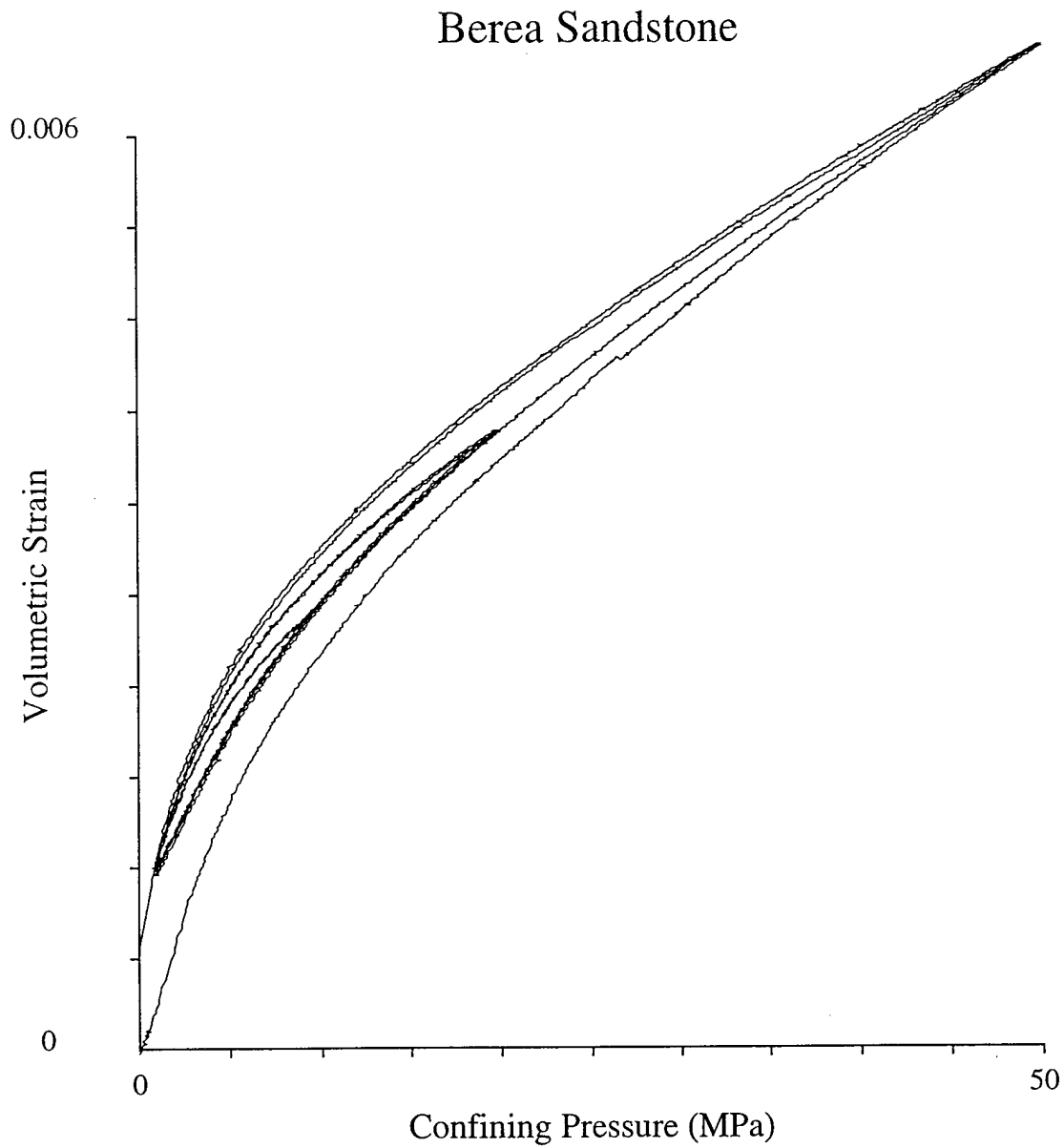


Figure 12: Volumetric strain versus confining pressure (mean stress) for Berea sandstone during the loading sequence in figure 11. Note the strong hysteresis here in contrast to the lack of hysteresis in the mean stress versus volumetric strain relationship during uniaxial stress cycling (compare with figure 8c).

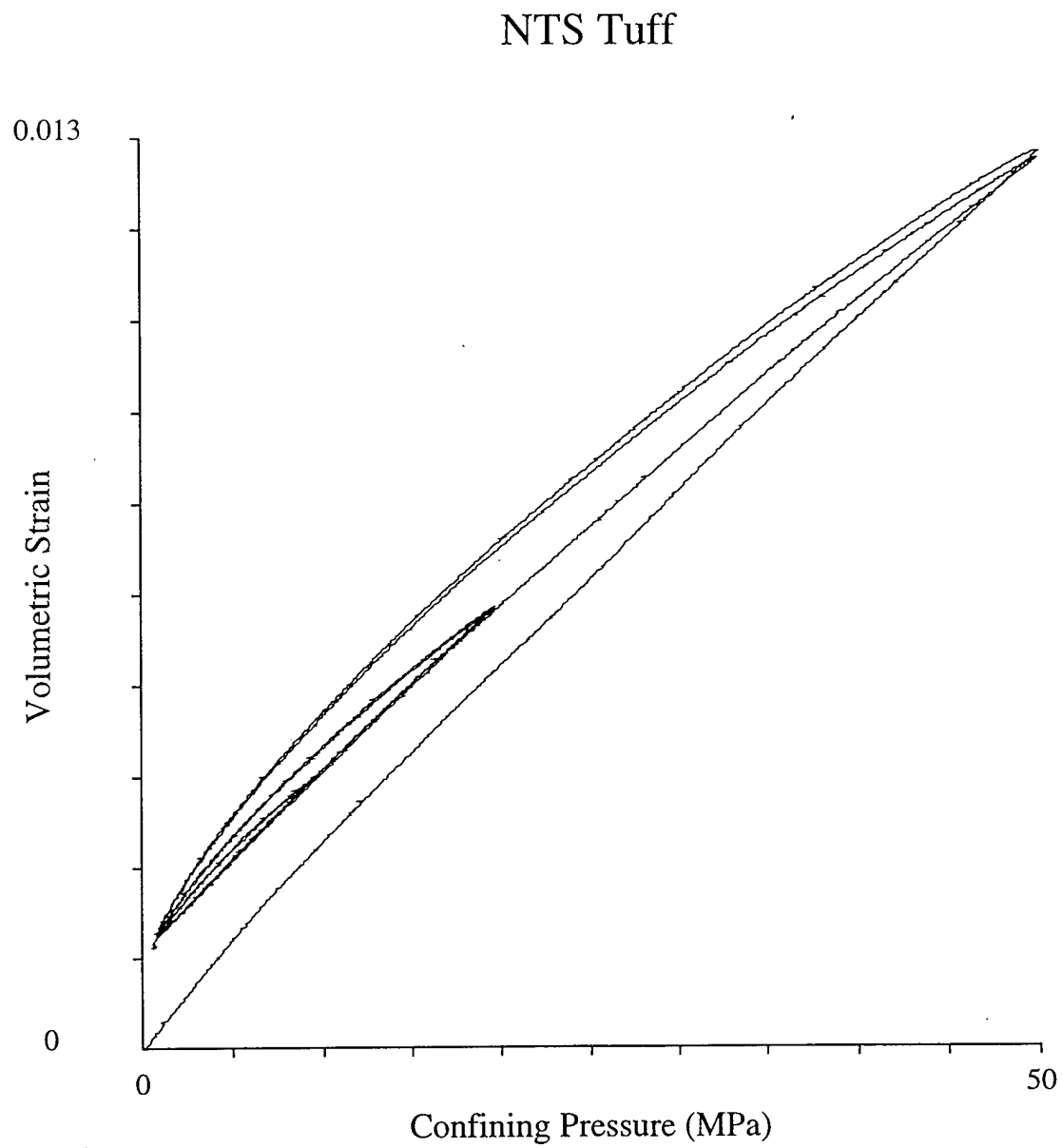


Figure 13: Volumetric strain versus confining pressure (mean stress) for N-Tunnel tuff during the loading sequence in figure 11.

## Sierra White Granite

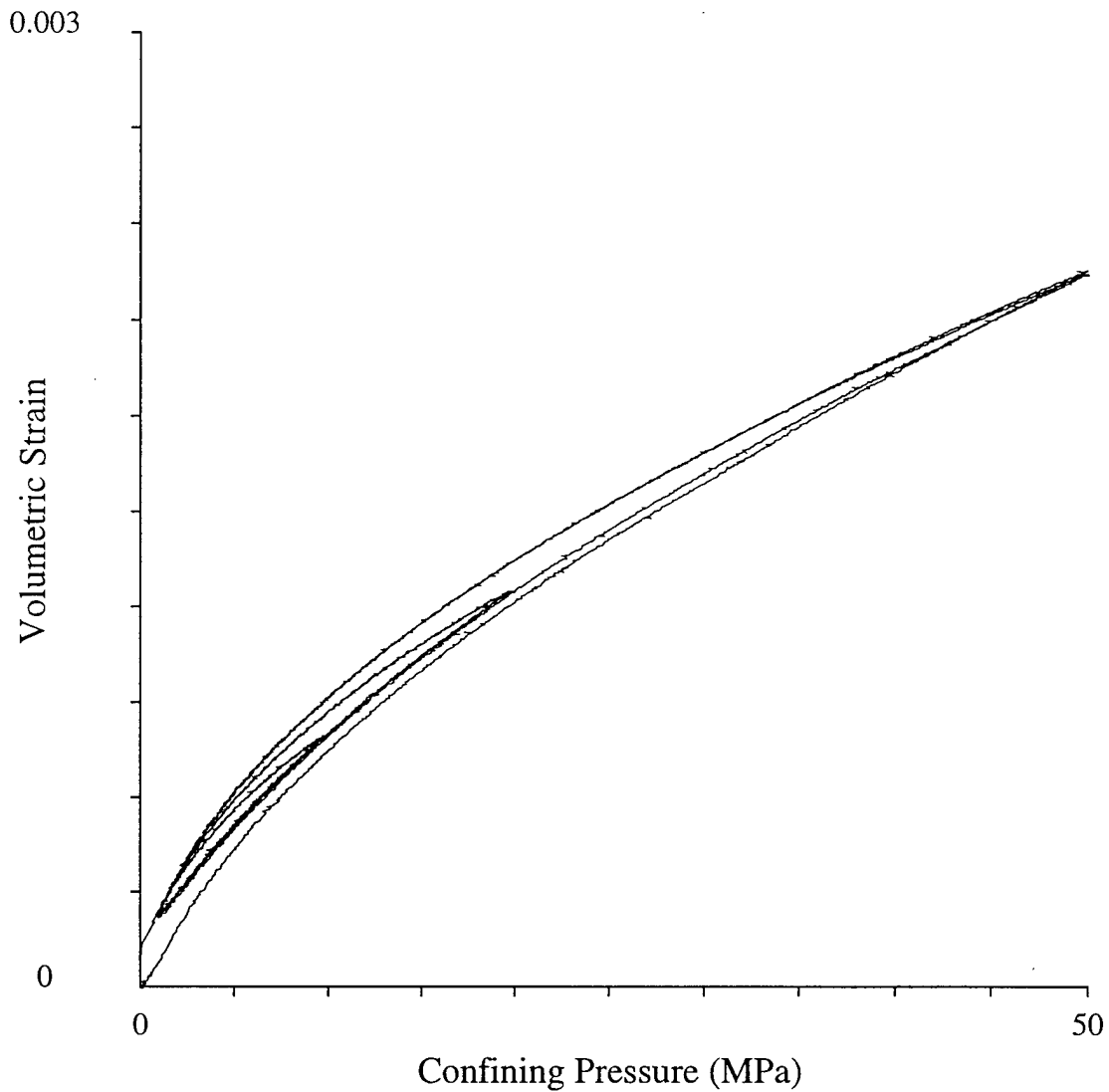


Figure 14: Volumetric strain versus confining pressure (mean stress) for Sierra White granite during the loading sequence in figure 11. Note the strong hysteresis here in contrast to the lack of hysteresis in the mean stress versus volumetric strain relationship during uniaxial stress cycling (compare with figure 10c).



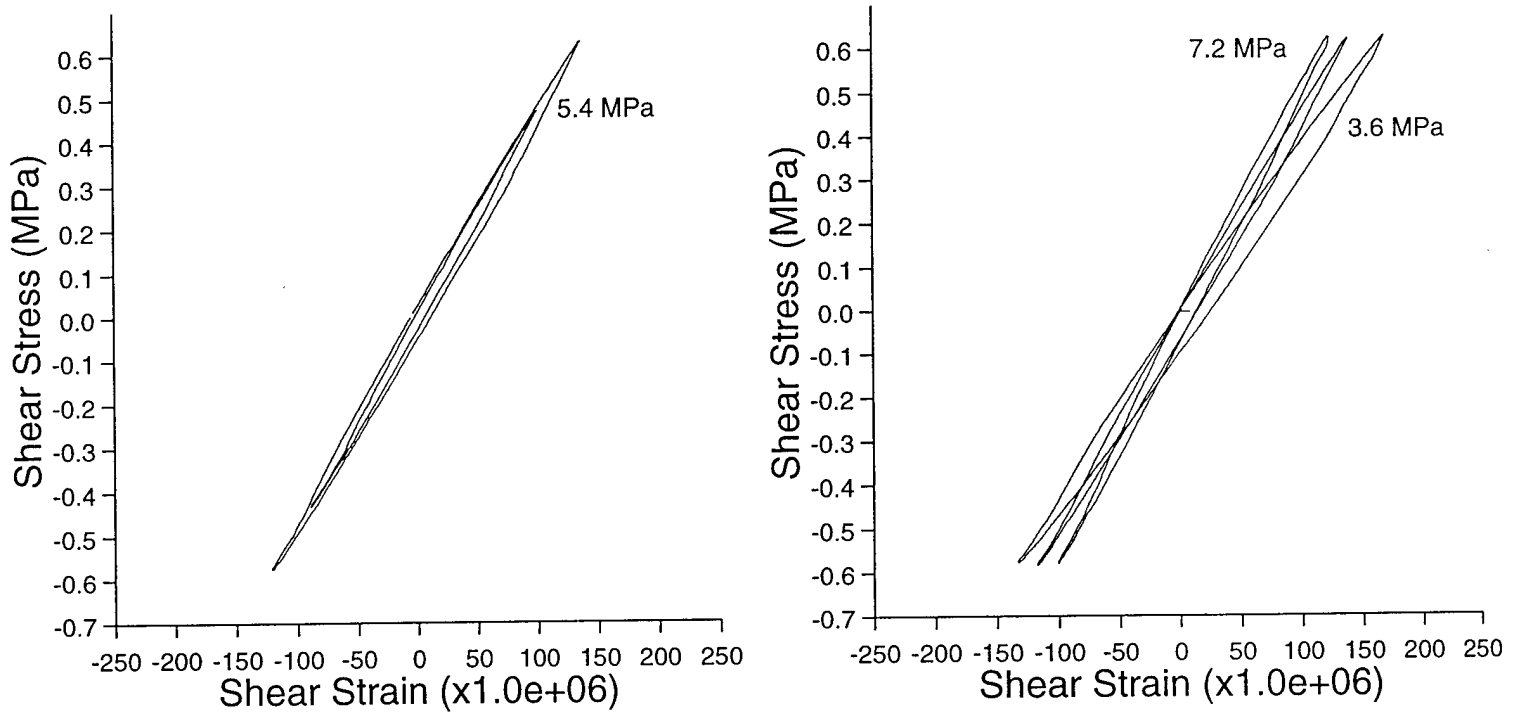


Figure 15: Measured shear stress versus shear strain for Berea sandstone. In the left figure, the effect of shear stress oscillation amplitude is shown at constant axial load (5.4 MPa). Note that the smaller loop is nested within and rotated with respect to the larger loop. In the right figure, the effect of normal load is illustrated, with loops at three different normal loads (3.6, 5.4, and 7.2 MPa). Note that the shear modulus increase and the loop width decreases with increasing normal load.

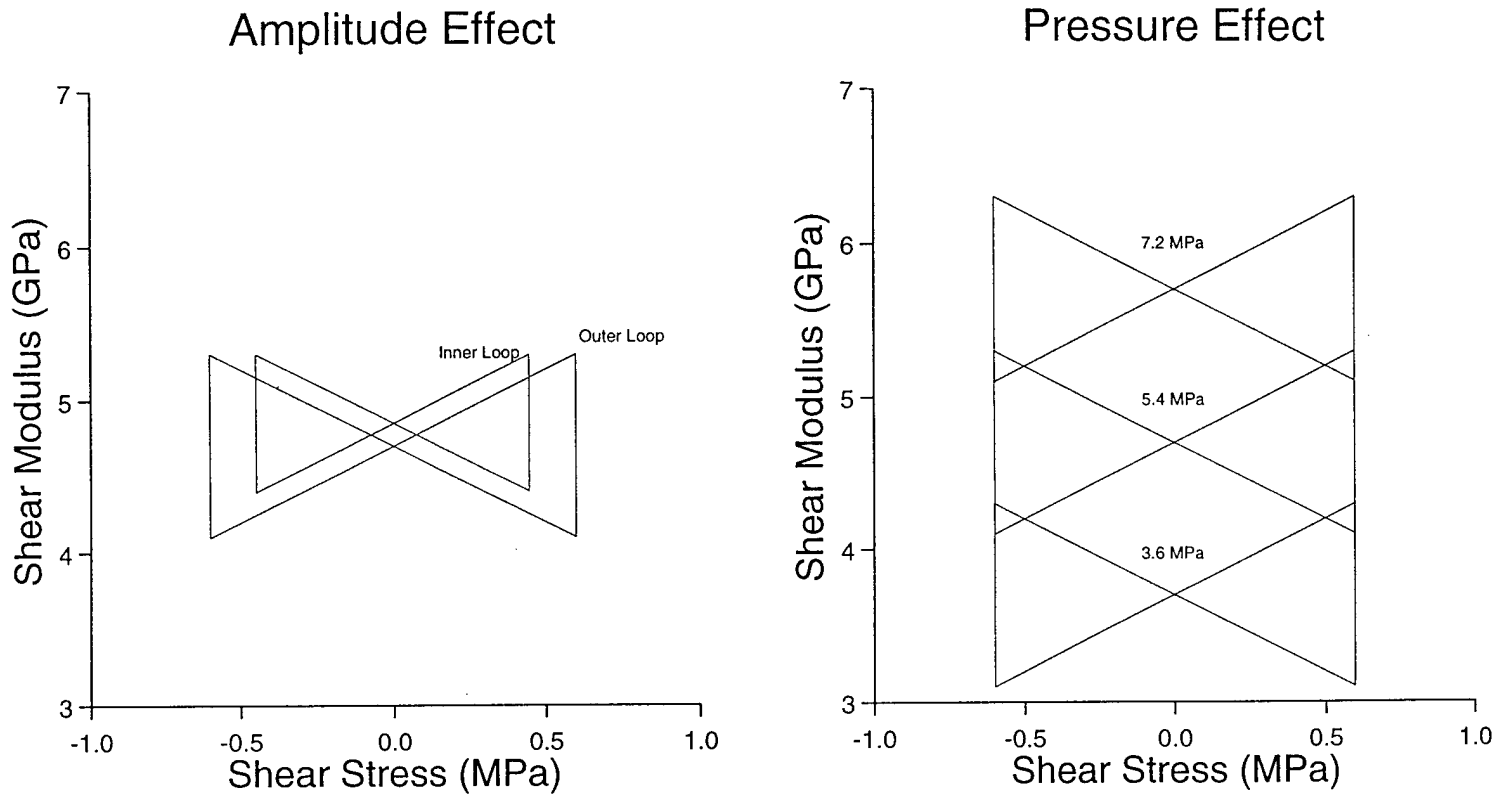


Figure 16: An illustration of the simple "bow-tie" rheology used to model the data. In the "bow-tie" example, the shear modulus is assumed to follow the form  $G = G' - A \cdot |\tau - \tau_r|$ , where  $G'$  is a function of the axial load ( $\sigma_{11}$ ),  $\tau$  is the shear stress, and  $\tau_r$  is the shear stress at the last reversal in loading direction.

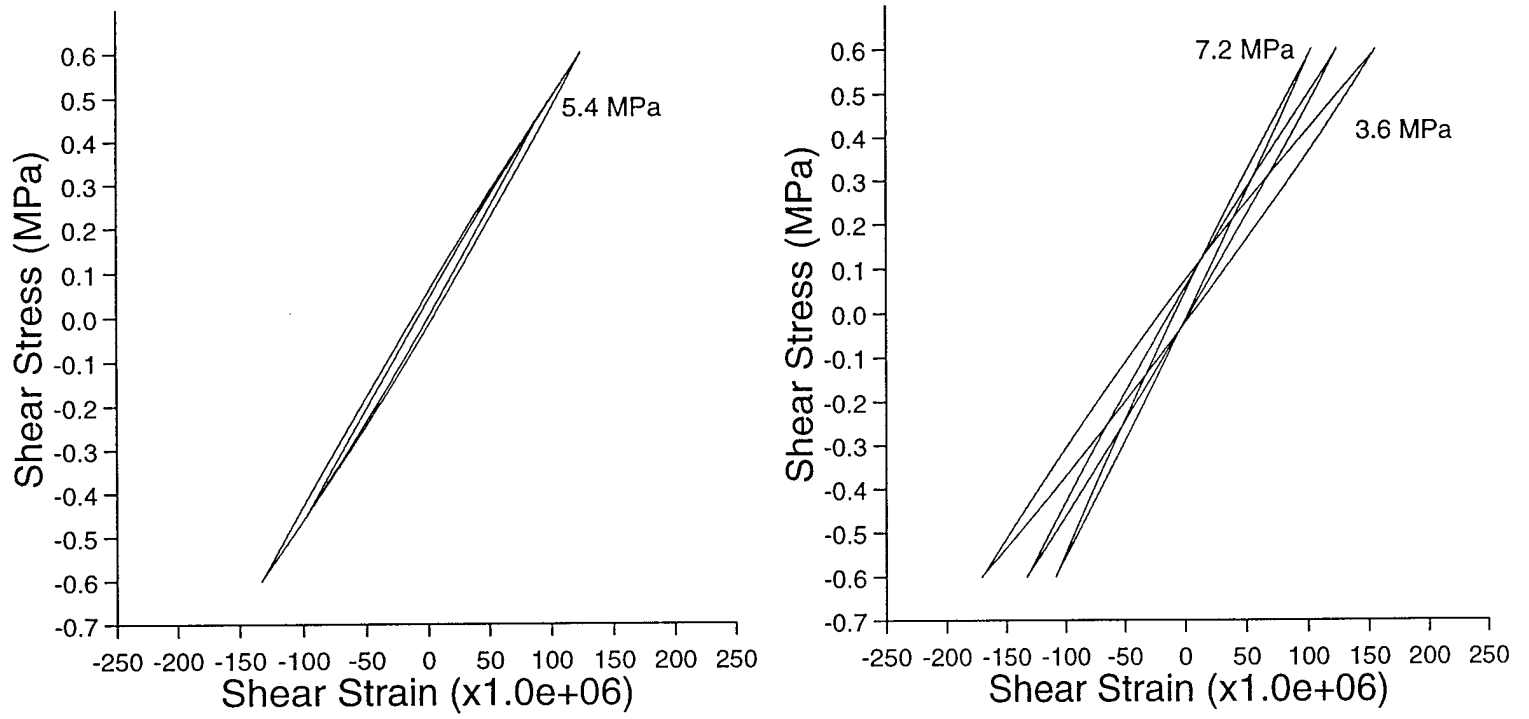


Figure 17: Predicted shear stress versus shear strain for Berea sandstone experiments in Figure 4. A simple "bow-tie" rheology was used to model the data. The model does a good job in producing both the amplitude and axial stress dependence of the deformation. All the data was modeled using  $G' = 2520 + 555\sigma_{11}$  (where  $G'$  and  $\sigma_{11}$  are in MPa), and  $A = 0.001$  is assumed constant.

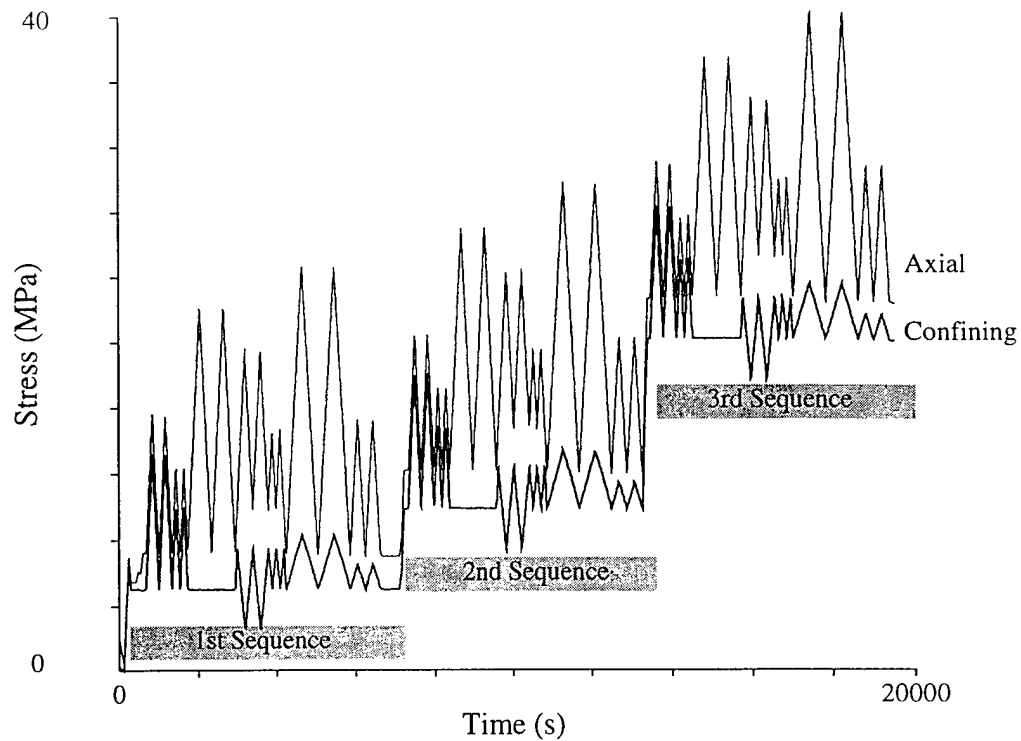


Figure 18: Loading protocol of an experiment designed to characterize the nonlinear, hysteretic rheology of rock. The protocol involves repeated execution of a sequence of loading modes, including perturbations in mean stress, uniaxial stress, shear stress, and uniaxial strain. See detail in Figure 19.

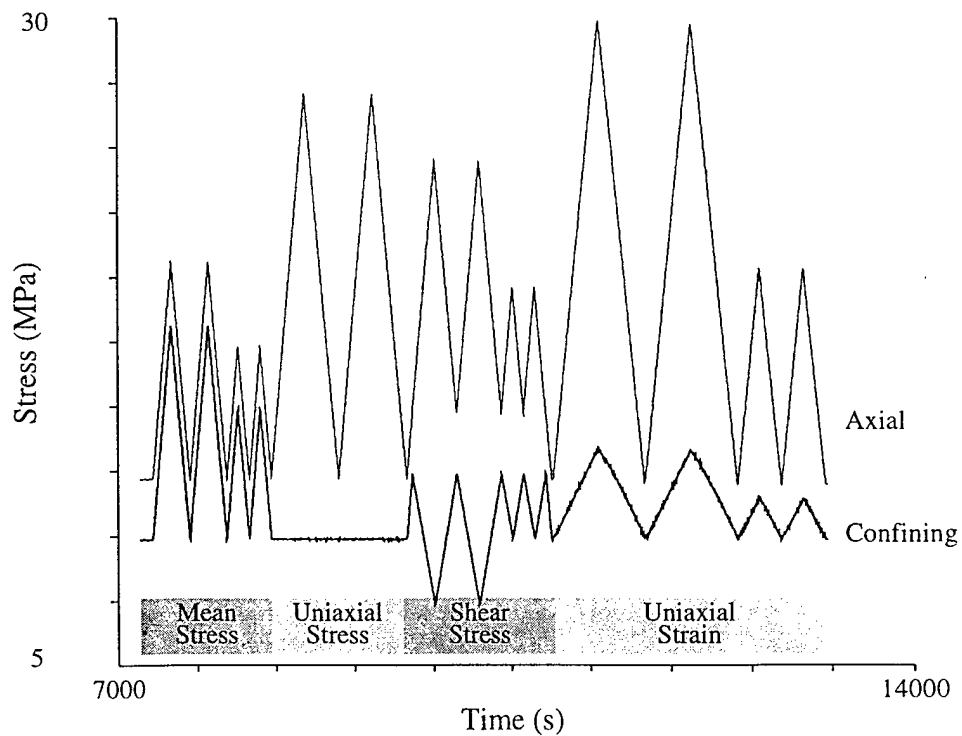


Figure 19: Detail of the loading sequence used in the experiment in Figure 18. Amplitudes of the various perturbations produce similar deviations in the shear and mean stresses.

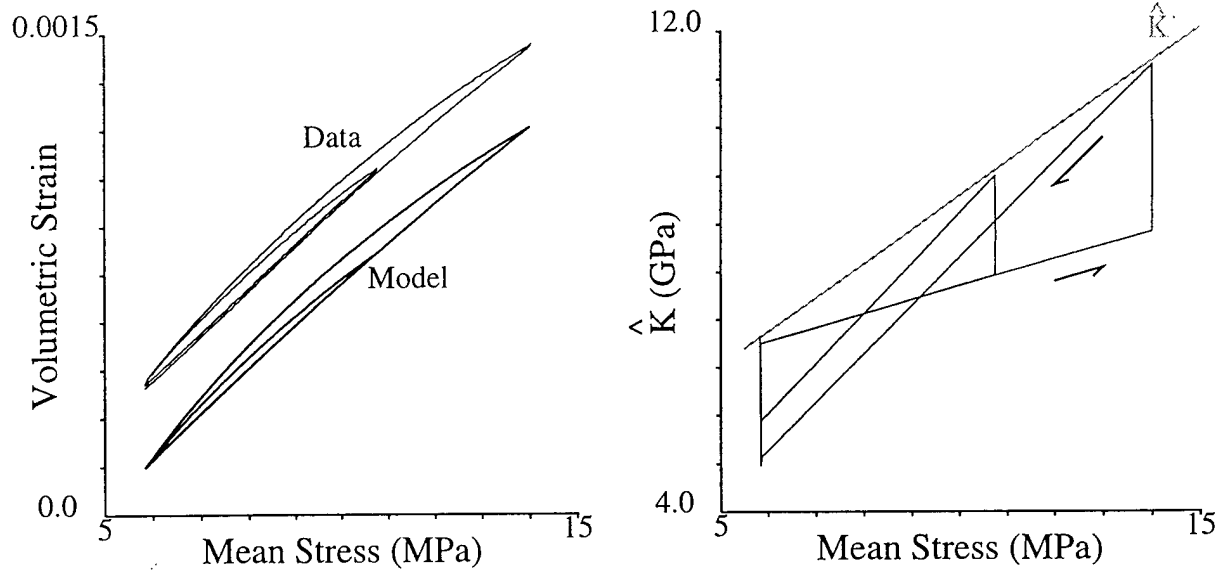


Figure 20: Comparison of stress-strain data and model predictions for a mean stress perturbation on Berea sandstone (left figure). The ABP parameterization is shown graphically in the right figure. The local modulus ( $\hat{K}$ ) changes linearly with stress during monotonic loading and/or unloading. At each reversal in loading direction, the local modulus reverts to a value of  $\hat{K}'$ , which is again a linear function of stress. The model is constrained by equation 3 to enforce discrete memory.

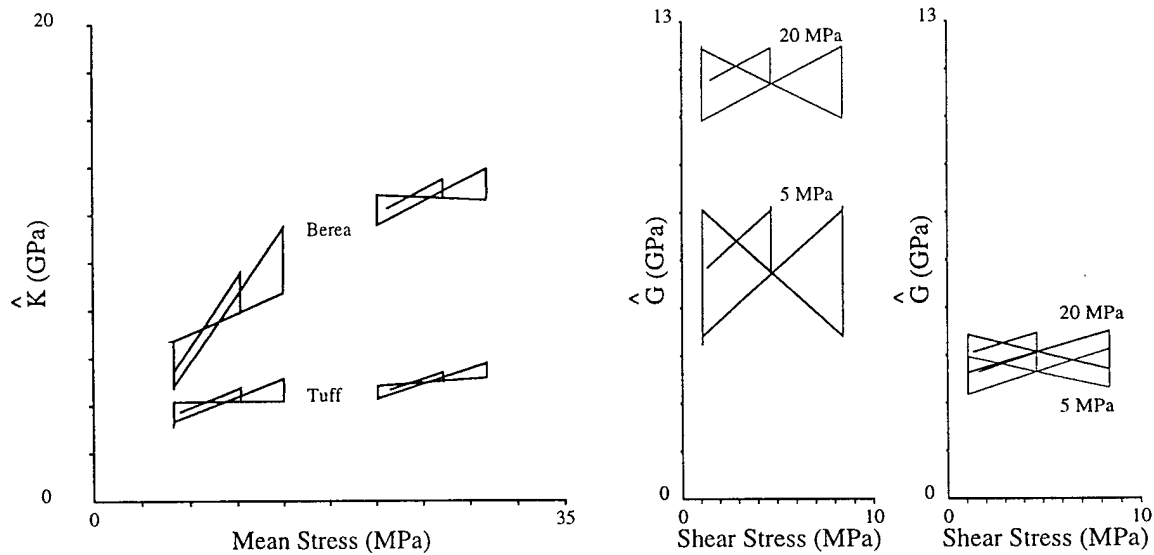


Figure 21: Model results for Berea sandstone and NTS tuff illustrating the dependence of model parameters on mean stress. Models results for mean stress perturbations are shown in the left figure (for a detailed example see Figure 20). Fits are to data from the mean stress perturbations during the 1st and 3rd sequence in Figure 18. The other figures (center  $\rightarrow$  Berea; right  $\rightarrow$  Tuff) illustrate the inferred shear rheology, again for the 1st and 3rd sequence in Figure 18. While the ABP holds for moderate perturbations in stress, large perturbations require a functionally more complex parameterization. This is particularly true for Berea sandstone, which exhibits a large mean stress dependence.

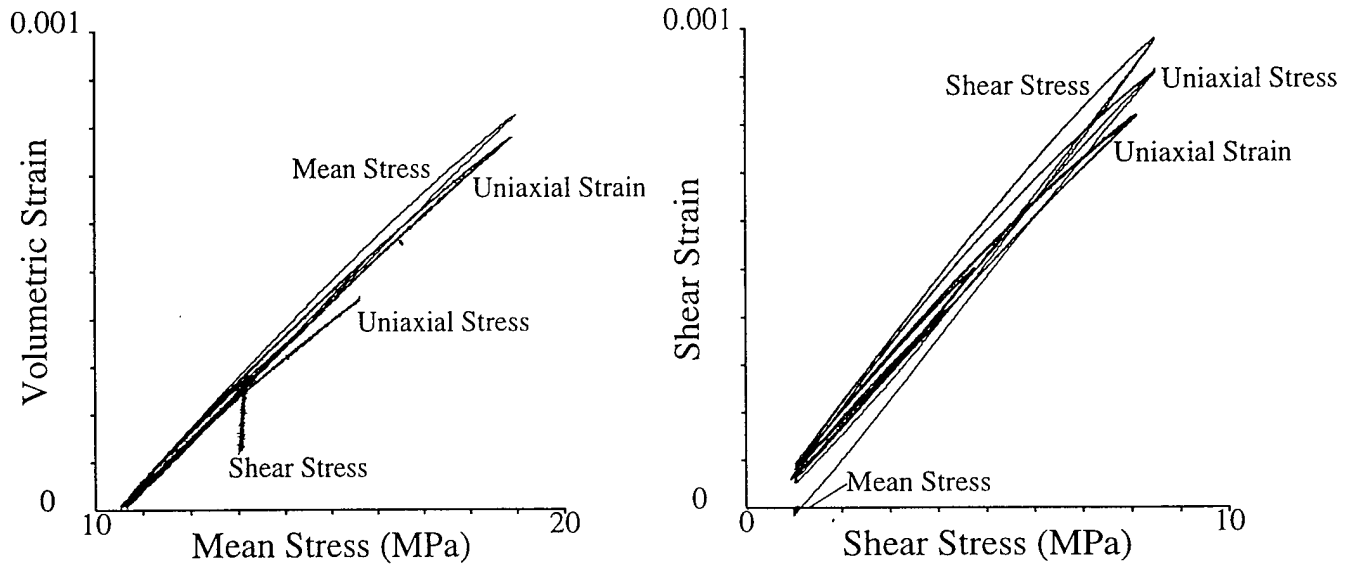


Figure 22: Volumetric strain versus mean stress and shear strain versus shear stress for Berea during the second loading sequence in Figure 18. Note that the shear stress produces a significant dilation. Note also that the pure mode stress strain response is not reproduced during mixed mode loading cycles for either the shear or the mean stress cases.

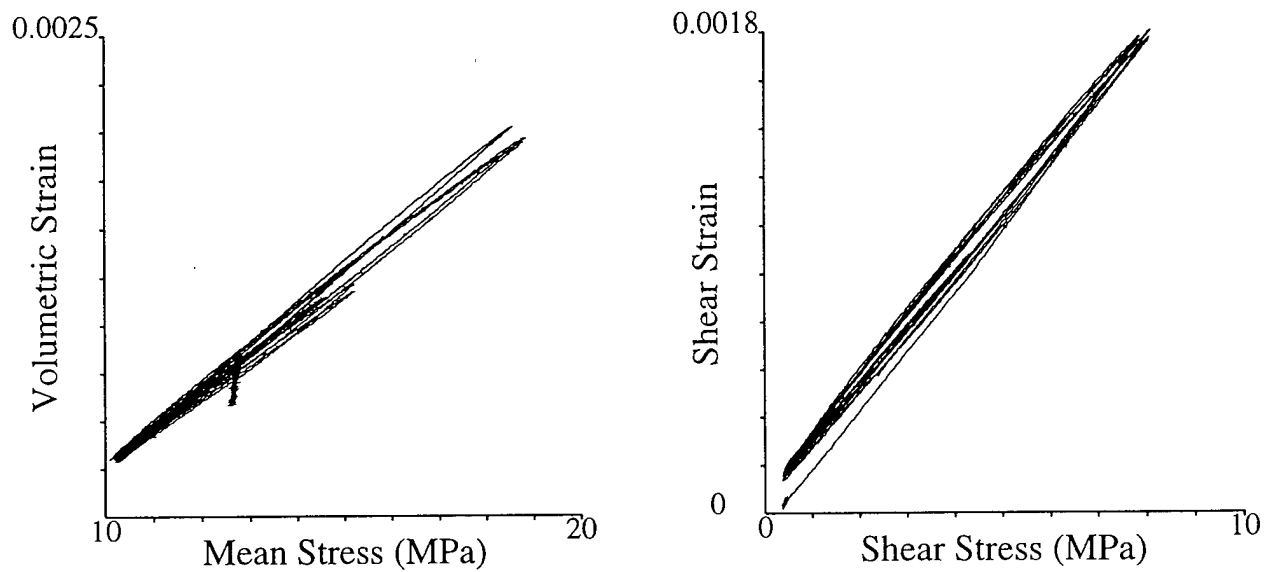


Figure 23: Volumetric strain versus mean stress and shear strain versus shear stress for N-Tunnel tuff during the second loading sequence in Figure 18. Note that the stress versus strain response is qualitatively similar to that of Berea (compare with Figure 22), but that many of the nonlinear effects are not as exaggerated.

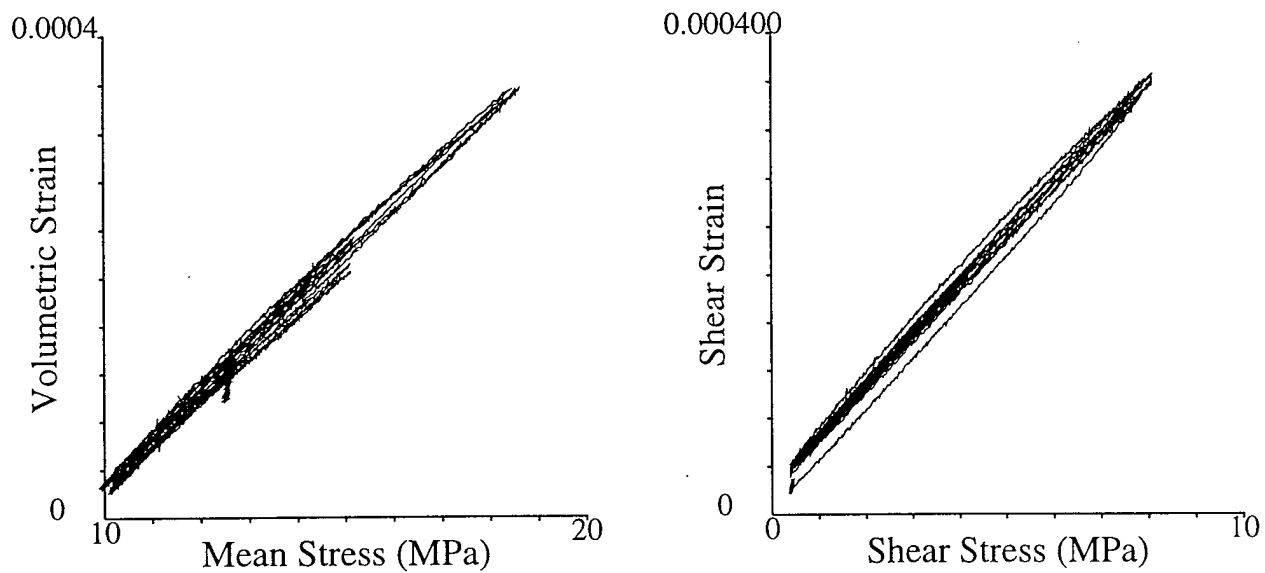


Figure 24: Volumetric strain versus mean stress and shear strain versus shear stress for Sierra White granite during the second loading sequence in Figure 18. Note that the stress versus strain response is qualitatively similar to that of Berea (compare with Figure 22), but that many of the nonlinear effects are not as exaggerated.



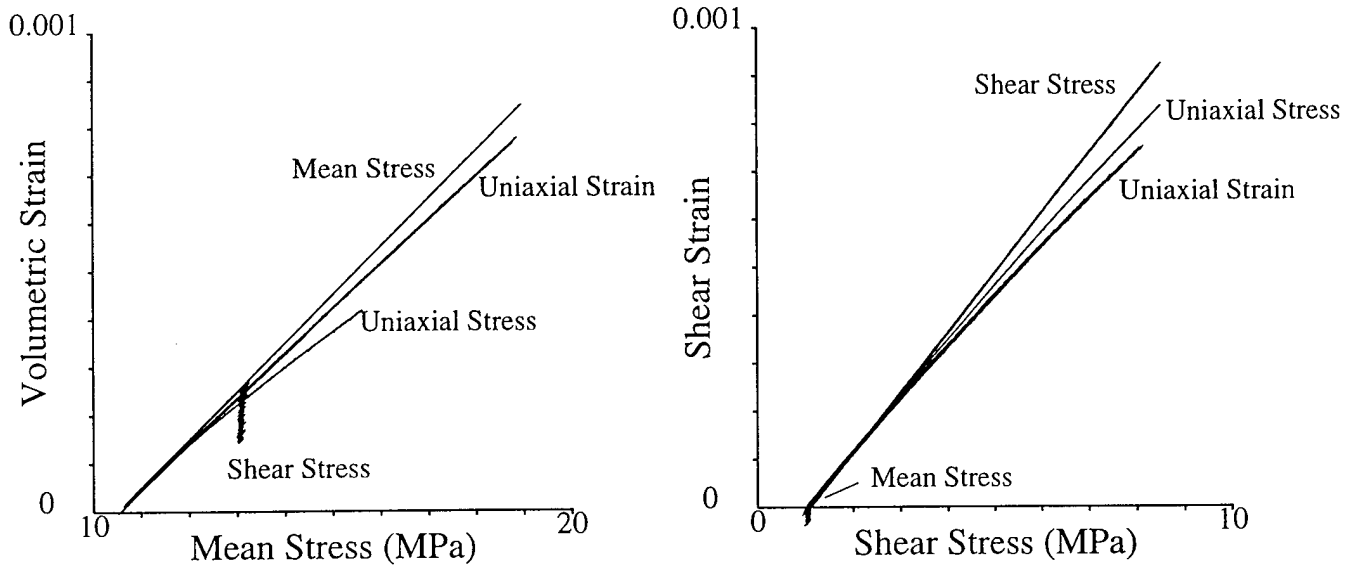


Figure 25: Predictions of the nonlinear elastic model for the data in Figure 22. Note the general agreement between the model (equations 4a-d) and the data for the entire loading sequence.

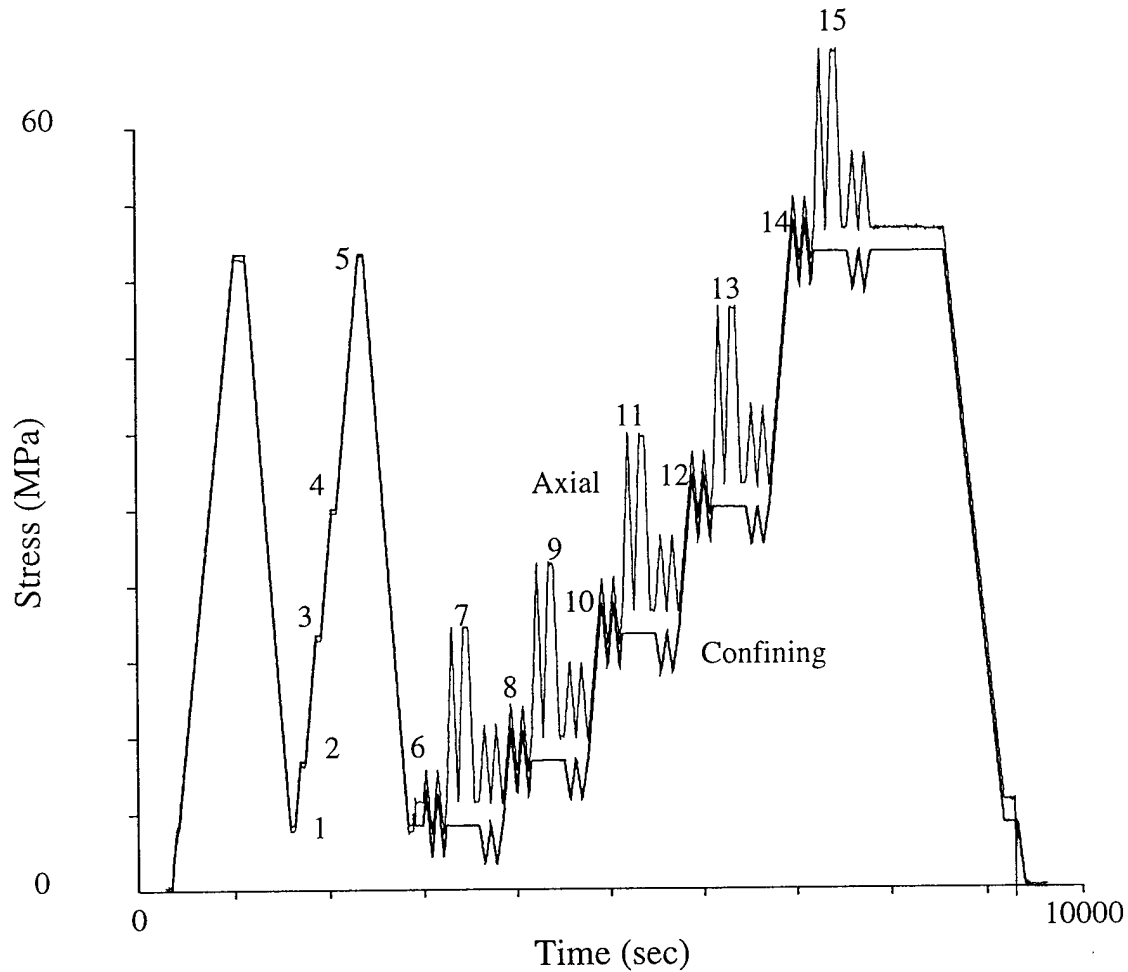


Figure 26: Loading protocol for an experiment designed to integrate the moderate strain rheology with ultrasonic velocity data. Following two cycles in hydrostatic confining stress, as sequence of perturbations in stress is repeated five times from five different starting stresses. Perturbation sequences consisted of cycles in mean stress, uniaxial stress, and shear stress. Numbers indicates points in the loading sequence where ultrasonic velocities were measured.

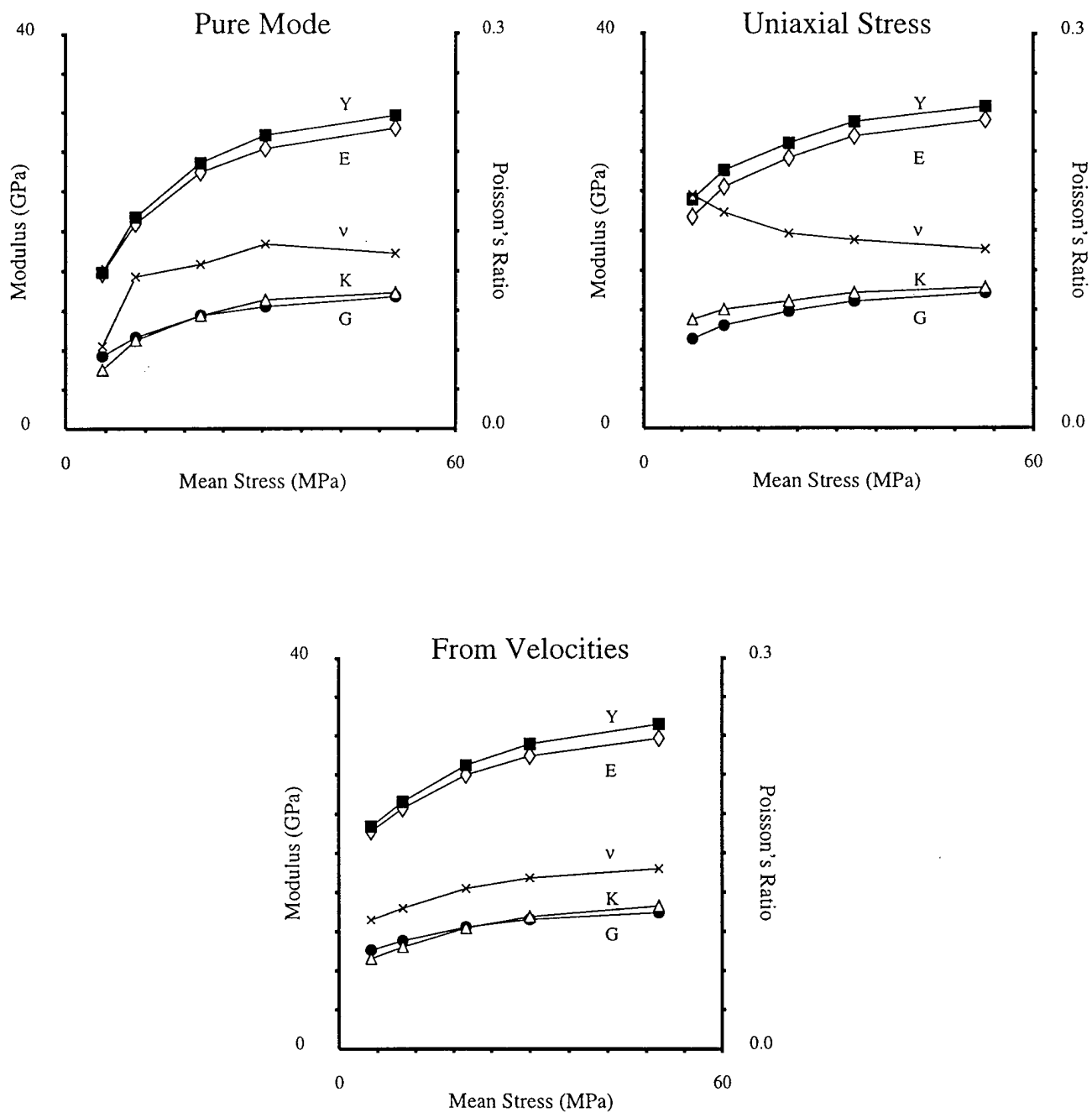


Figure 27: Inferred elastic constants determined from: a) [top left] pure mode measurements of  $\langle \hat{K}_\sigma \rangle$  and  $\langle \hat{G}_\tau \rangle$ ; b) [top right] measurements of  $\langle \hat{E}_{us} \rangle$  and  $\langle \hat{\nu}_{us} \rangle$  from uniaxial stress perturbations; and c) [bottom center] ultrasonic compressional and shear wave velocities under hydrostatic compression (i.e. points 1-5 in Figure 26).

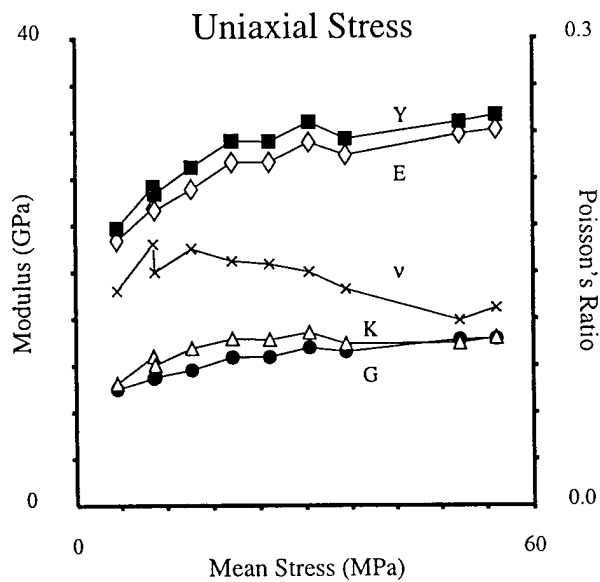
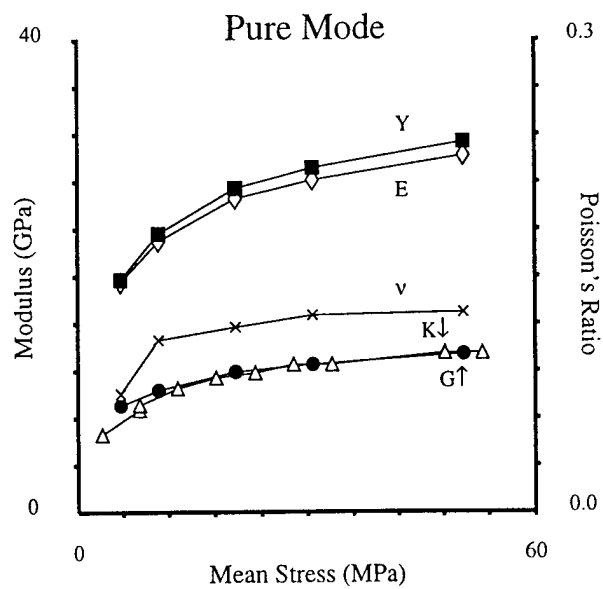


Figure 28: Inferred elastic constants determined from: (a) [top] pure mode measurements of  $\hat{K}'_{\sigma}$  and  $\hat{G}'_{\tau}$ ; and (b) [bottom] measurements of  $\hat{E}'_{us}$  and  $\hat{\nu}'_{us}$  from uniaxial stress perturbations.

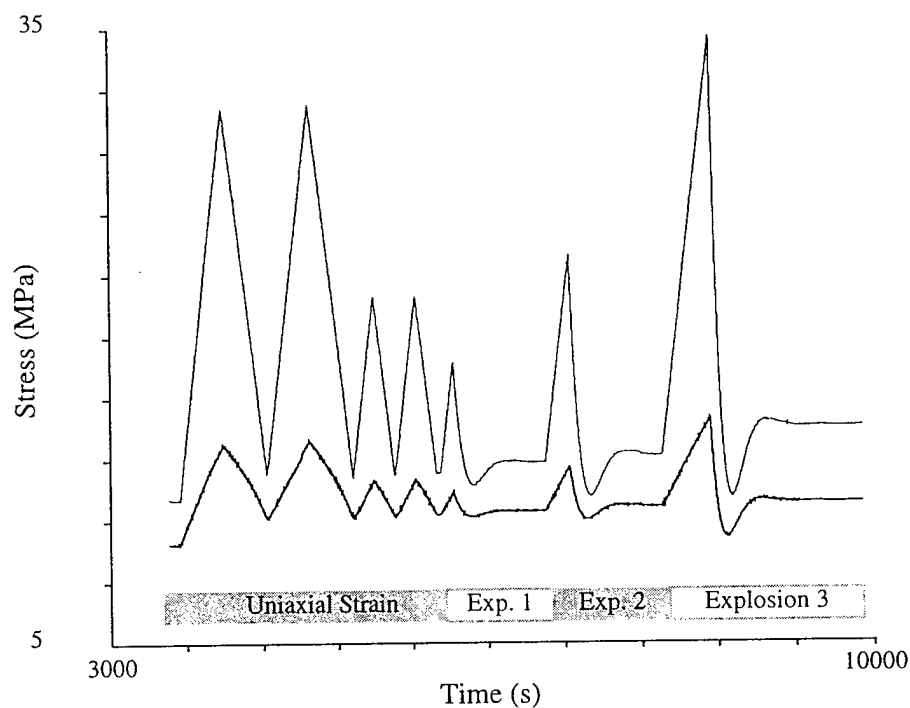


Figure 29: Loading protocol during an experiment designed to characterize a simplified rheology for the case of a spherically propagating compressional wave. Uniaxial strain perturbations are followed by three "explosion like" loading paths of increasing amplitude.

## Berea

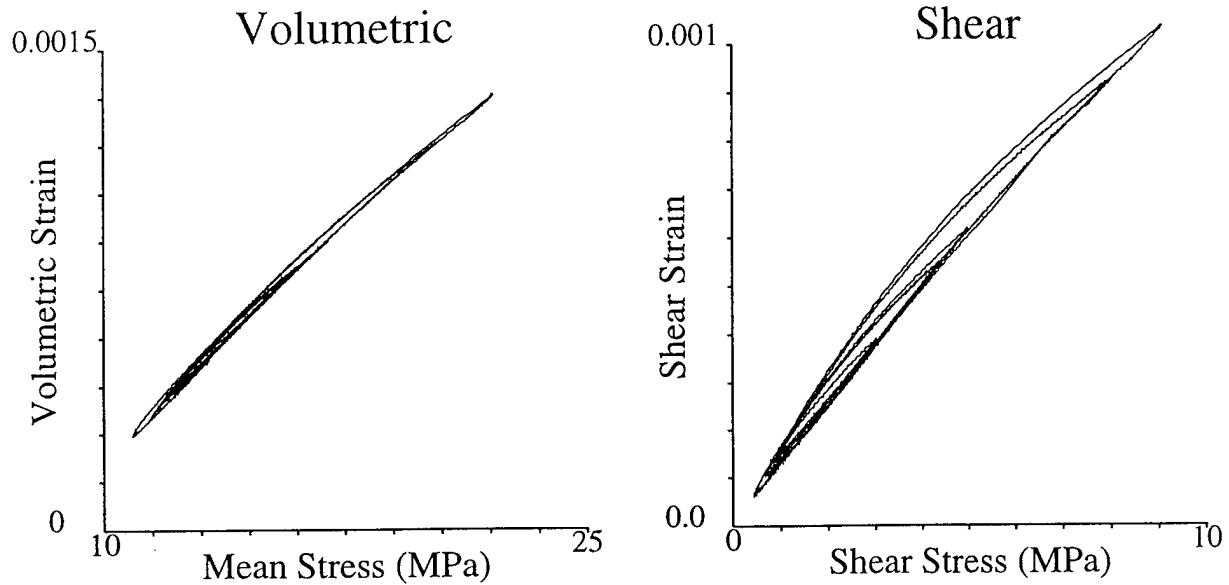


Figure 30: Volumetric strain versus mean stress and shear strain versus shear stress for Berea sandstone during the loading protocol in Figure 29. Note the well behaved nature of the hysteresis and nonlinearity, exhibiting the characteristic shape and "nested loop" behavior of the ABP.

## N-Tunnel Tuff

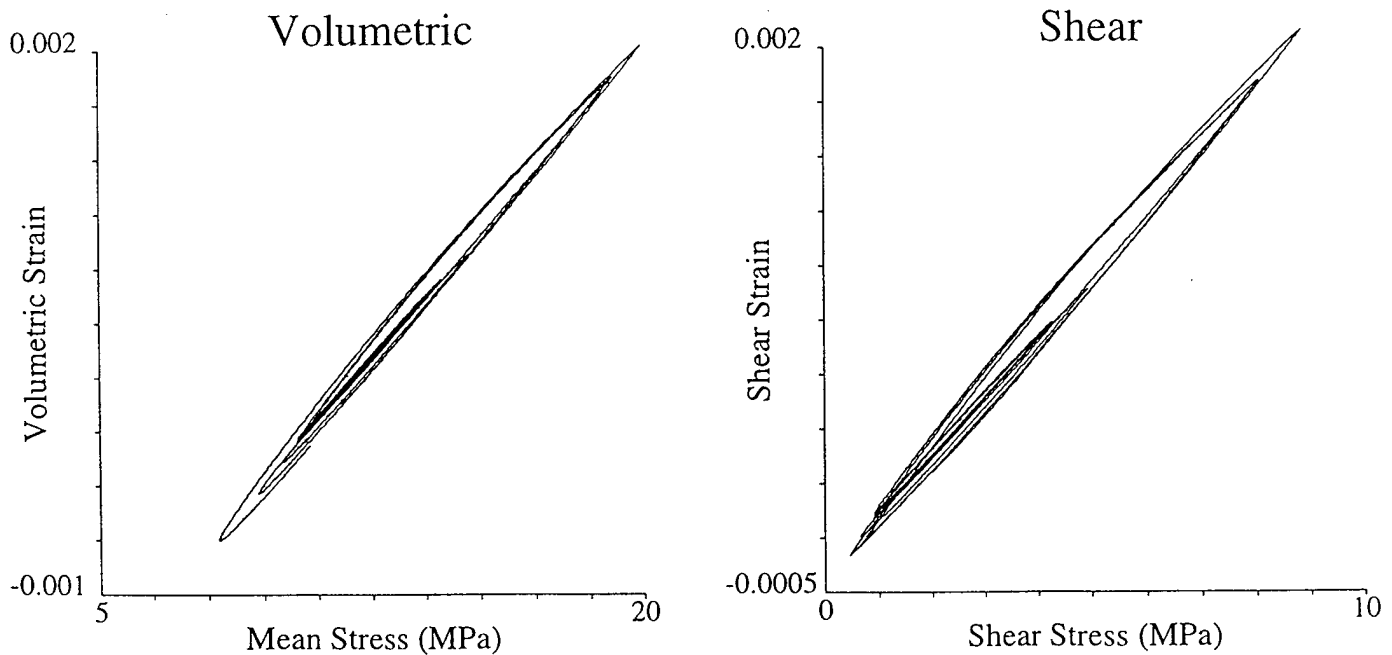
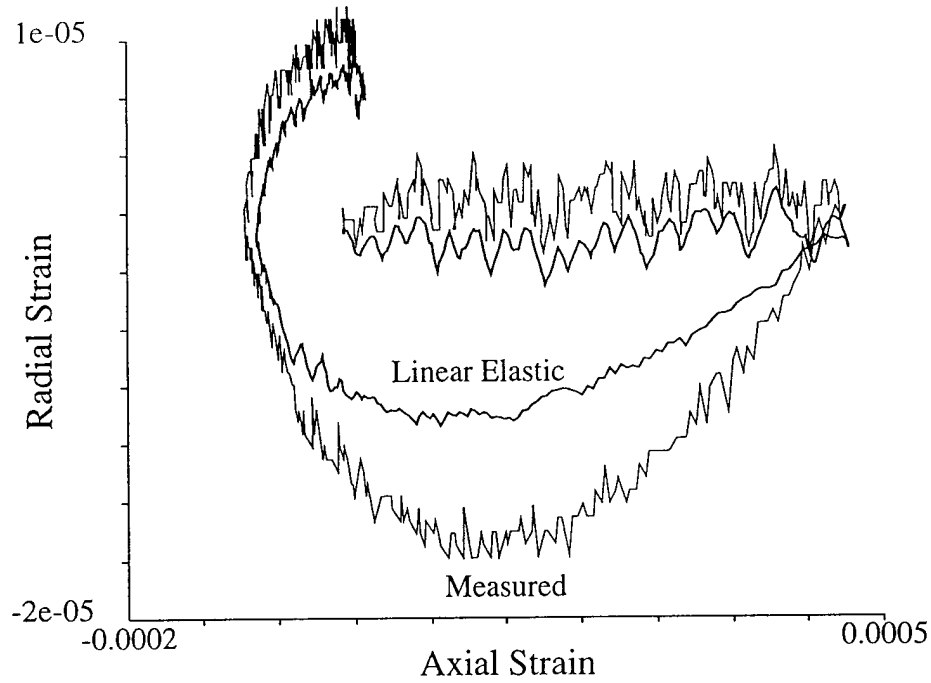


Figure 31 Volumetric strain versus mean stress and shear strain versus shear stress for N-Tunnel tuff during the loading protocol in Figure 29. Note the well behaved nature of the hysteresis and nonlinearity, exhibiting the characteristic shape and "nested loop" behavior of the ABP.

### Exp. 2



### Exp. 3

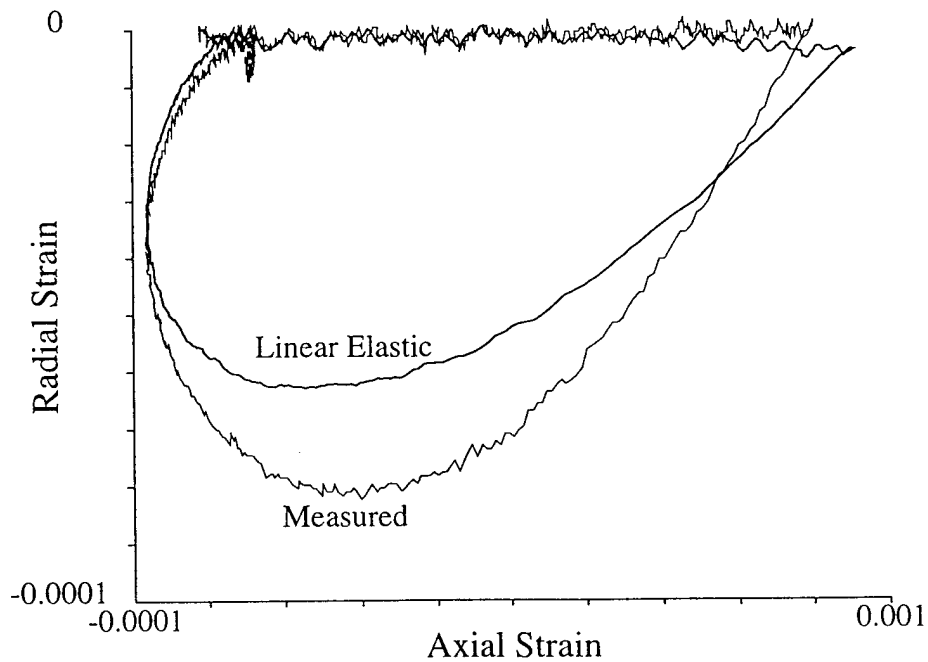


Figure 32: Strain path measured during the 2nd and 3rd "explosions" as shown in Figure 6. The predictions for a linear elastic solid (with elastic constants constrained to fit the uniaxial strain loading), are shown for comparison. While qualitatively similar, systematic differences arise from the nonlinearity and hysteresis which may have a significant effect on wave propagation and/or the interpretation of a source function.

## Berea: High Amplitude Explosion

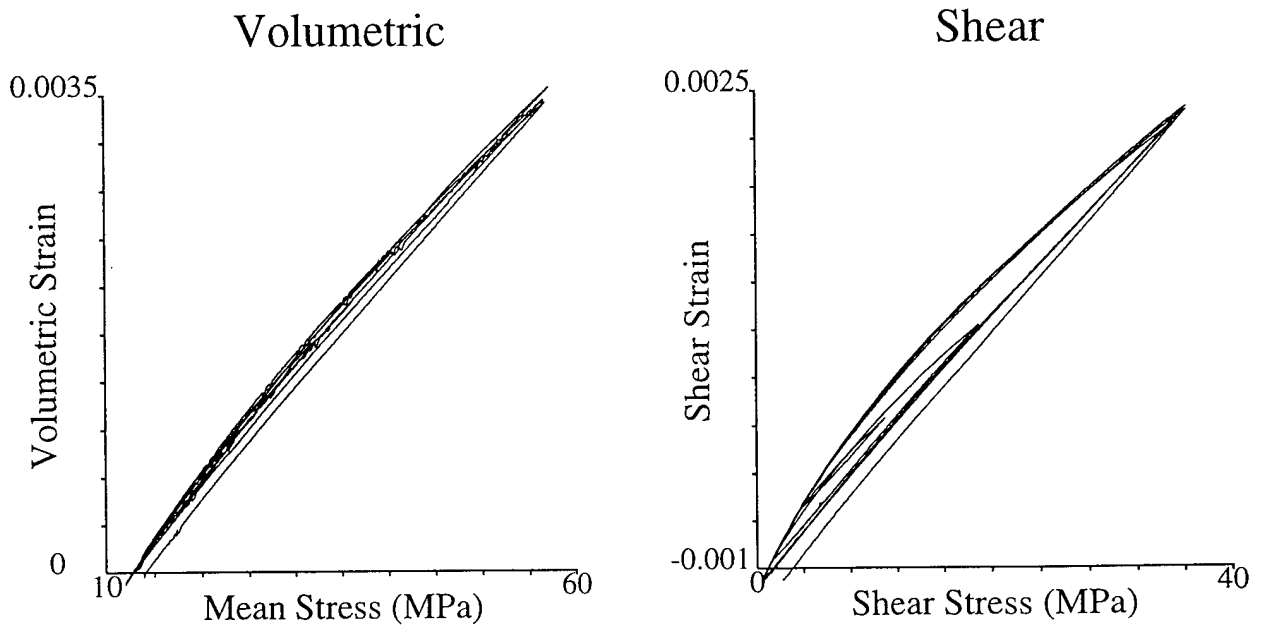


Figure 33: Stress versus strain relationship for Berea sandstone during uniaxial strain cycling similar to that in Figure 29, but with peak stress amplitudes 4 times higher. Note the similarity with Figure 30, indicating that the rheology does not change even at considerably higher strain amplitude conditions.



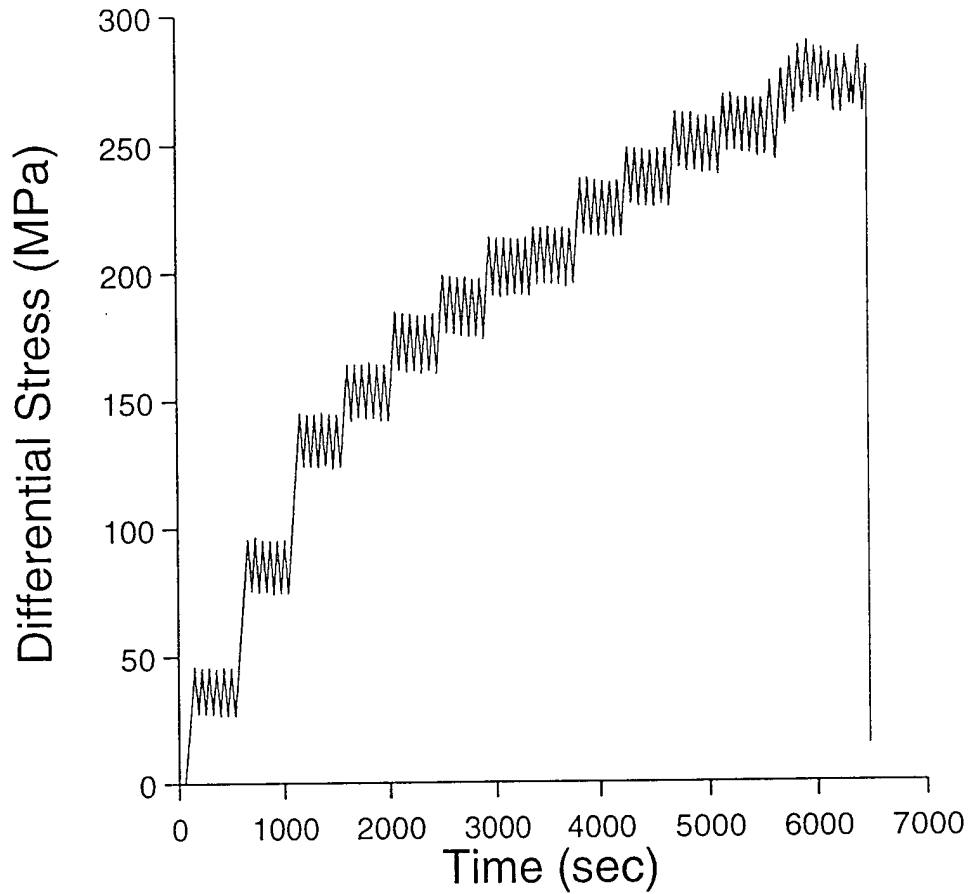


Figure 34: Loading protocol for an experiment designed to probe the transition into the damage regime. At a series of increasing levels of axial load (at fixed confining pressure), small perturbations in axial load are performed to characterize the unloading modulus and its time (and cycle) dependence. The axial load is increased until failure occurs.

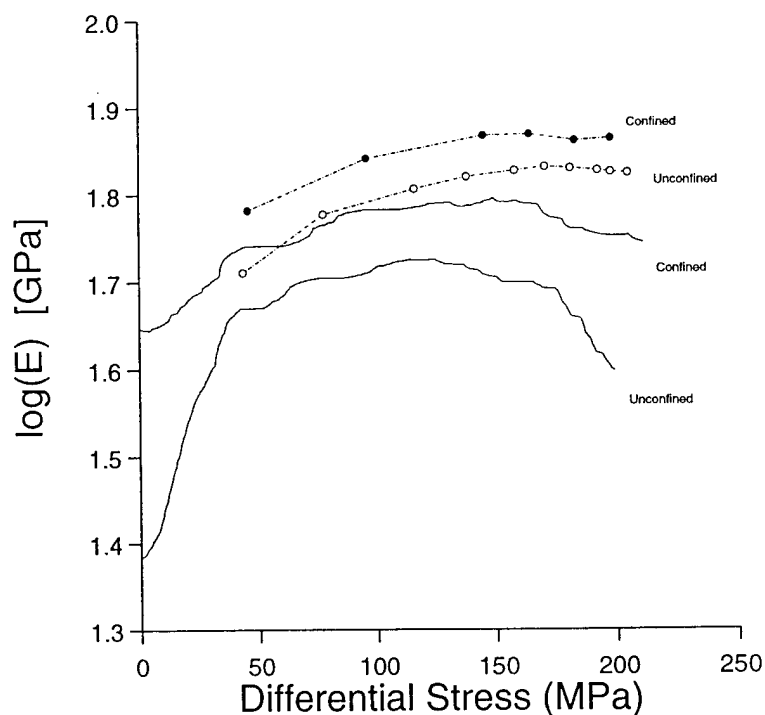
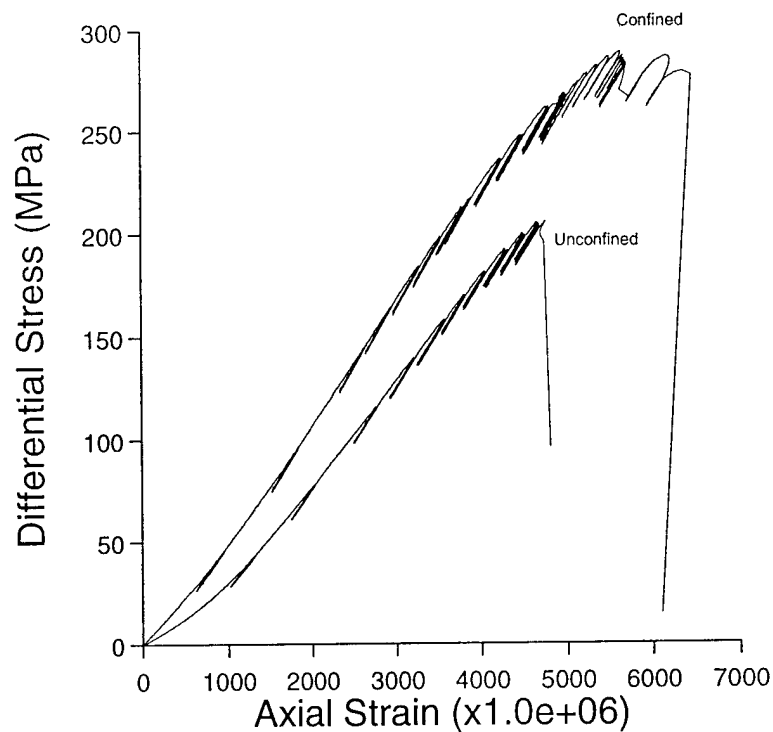


Figure 35: a) Stress strain data from two uniaxial compression experiments on Barre granite, one unconfined and the other at a fixed confining pressure of 10 MPa. During the loading, perturbations in axial load were performed to measure the unloading stiffness. b) The logarithm of the Young's modulus plotted as a function of differential stress. Solid lines indicating the modulus upon loading and the circles indicate the average modulus during the small cyclic perturbations.